

Tracing the origin of adult intestinal stem cells

Jordi Guiu^{1,14}, Edouard Hannezo^{2,3,14}, Shiro Yui^{1,13}, Samuel Demharter¹, Svetlana Ulyanchenko¹, Martti Maimets¹, Anne Jørgensen⁴, Signe Perlman⁵, Lene Lundvall⁵, Linn Salto Mamsen⁶, Agnete Larsen⁷, Rasmus H. Olesen⁷, Claus Yding Andersen⁶, Lea Langhoff Thuesen⁸, Kristine Juul Hare⁸, Tune H. Pers⁹, Konstantin Khodosevich¹, Benjamin D. Simons^{2,10,11} & Kim B. Jensen^{1,12*}

Adult intestinal stem cells are located at the bottom of crypts of Lieberkühn, where they express markers such as LGR5^{1,2} and fuel the constant replenishment of the intestinal epithelium¹. Although fetal LGR5-expressing cells can give rise to adult intestinal stem cells^{3,4}, it remains unclear whether this population in the patterned epithelium represents unique intestinal stem-cell precursors. Here we show, using unbiased quantitative lineage-tracing approaches, biophysical modelling and intestinal transplantation, that all cells of the mouse intestinal epithelium—irrespective of their location and pattern of LGR5 expression in the fetal gut tube—contribute actively to the adult intestinal stem cell pool. Using 3D imaging, we find that during fetal development the villus undergoes gross remodelling and fission. This brings epithelial cells from the non-proliferative villus into the proliferative intervillus region, which enables them to contribute to the adult stem-cell niche. Our results demonstrate that large-scale remodelling of the intestinal wall and cell-fate specification are closely linked. Moreover, these findings provide a direct link between the observed plasticity and cellular reprogramming of differentiating cells in adult tissues following damage^{5–9}, revealing that stem-cell identity is an induced rather than a hardwired property.

The intestine forms from the pseudostratified gut tube, which becomes patterned during late fetal development into villi and a continuous intervillus region formed by LGR5[–] and LGR5⁺ cells, respectively¹⁰ (Fig. 1a, Extended Data Fig. 1a–c). The continuous intervillus region is the major site of proliferation in the developing intestine (Extended Data Fig. 1d–f), and crypts subsequently form from this region postnatally¹¹. Despite the apparent transcriptional similarity between fetal and adult LGR5⁺ cells⁴, it remains unclear how the fetal immature intestine transitions into the mature structure and how this is orchestrated at the cellular level. In particular, it is not known whether a specialized subset of fetal cells becomes adult intestinal stem cells or whether stem-cell identity is an induced property.

To investigate the role of fetal LGR5⁺ cells in the establishment of the adult intestinal stem cell population, we performed lineage tracing on this population from embryonic day (E)16.5. Focusing on the proximal part of the small intestine, we observed that, consistent with previous reports^{3,4,12}, progeny of the LGR5-expressing population were maintained into adulthood and thereby contributed to the adult intestinal stem-cell compartment (Fig. 1b). Most of the clones observed at postnatal day (P)0 were, as expected, located in the intervillus regions (Extended Data Fig. 2a). Moreover, it was not until P11 that clones extended as ribbons from the base of crypts to the tips of villi (Supplementary Video 1).

The quantitative contribution from LGR5⁺ progeny, labelled at E16.5, was slightly greater than the overall degree of tissue expansion (Fig. 1c, Extended Data Fig. 2b–e). This confirmed that LGR5⁺ cells were an important source of tissue growth. However, given that LGR5⁺ cells constituted only a small fraction of the cells (fraction of LGR5⁺ cells/total cells, $f = 7.0\% \pm 0.9\%$, mean \pm s.e.m.) in the proximal part of the small intestine at the time of labelling (Extended data Fig. 2f–h), we reasoned that if LGR5⁺ cells were the main source of adult epithelium (Fig. 1d) they would have to expand by a ratio $1/f$ greater than overall tissue to fuel growth and replace cells outside the intervillus regions. Thus, LGR5⁺ clones should expand 130-fold from P5 to adulthood, nearly an order of magnitude higher than the measured value (Fig. 1e). Expansion of LGR5⁺ progeny was thus insufficient to explain tissue growth.

To resolve the cellular diversity in the epithelium at E16.5, we performed single-cell RNA sequencing (scRNA-seq) analysis. Consistent with our characterization of LGR5–eGFP, *Lgr5* was detected in 7% of the 3,509 cells analysed and—despite detecting only goblet cells by immunostaining—we identified other differentiated cell types, including Paneth cells (*Lyz1*), entero-endocrine cells (*Chga*) and enterocytes (*Alpi*) (Extended Data Fig. 3a, b). In the adult epithelium, the differentiated villi compartment can be separated into at least five transcriptionally distinct populations¹³. In the fetal intestine, these largely collapse into two populations, and a gene signature for crypt proliferation was detected beyond the LGR5⁺ compartment, including cells expressing differentiation markers¹⁴ (Extended Data Fig. 3c–e). This strongly supported the conclusion that cells in the fetal intestinal epithelium were distinct from their adult counterparts, and that cells expressing differentiation markers had not completed their differentiation program.

To test experimentally how cells outside the intervillus region contributed to tissue growth, we performed fate mapping using a ubiquitously expressed keratin 19 (*Krt19*)-driven Cre model (Fig. 2a; Extended Data Fig. 3f–h). Although the scRNA-seq data revealed that 49% of *Krt19*-expressing cells at E16.5 score positive for the proliferation signature, the expansion of clones closely mirrored the overall growth of the tissue (Fig. 2b; Extended Data Fig. 3i), which confirms that *Krt19*-expressing cells were representative of the tissue. However, we found that both the long-term persistence (defined as the fraction of surviving clones) and size of KRT19-labelled clones were very similar to their LGR5-labelled counterparts (Fig. 2c, d, Supplementary Information, ‘Supporting clonal data’). Several independent measurements confirmed that KRT19 marked a population of cells distributed randomly along the villus–intervillus axis (Extended Data Fig. 3j, k, Supplementary Video 2). Moreover, apoptotic cells at the tips of villi appeared only from P7; this means that KRT19⁺ clones cannot be lost

¹Biotech Research and Innovation Centre (BRIC), University of Copenhagen, Copenhagen, Denmark. ²The Wellcome Trust–Cancer Research UK Gurdon Institute, University of Cambridge, Cambridge, UK. ³Institute of Science and Technology Austria, Klosterneuburg, Austria. ⁴Department of Growth and Reproduction, Rigshospitalet, University of Copenhagen, Copenhagen, Denmark. ⁵Department of Gynecology, Rigshospitalet, University of Copenhagen, Copenhagen, Denmark. ⁶Laboratory of Reproductive Biology, Section 5712, The Juliane Marie Centre for Women, Children and Reproduction, University Hospital of Copenhagen, University of Copenhagen, Copenhagen, Denmark. ⁷Department of Biomedicine–Pharmacology, Aarhus University, Aarhus, Denmark. ⁸Department of Obstetrics and Gynaecology, Hvidovre University Hospital, Hvidovre, Denmark. ⁹The Novo Nordisk Foundation Center for Basic Metabolic Research, Faculty of Health and Medical Sciences, University of Copenhagen, Copenhagen, Denmark. ¹⁰Cavendish Laboratory, Department of Physics, University of Cambridge, Cambridge, UK. ¹¹The Wellcome Trust–Medical Research Council Stem Cell Institute, University of Cambridge, Cambridge, UK. ¹²Novo Nordisk Foundation Center for Stem Cell Research, Faculty of Health and Medical Sciences, University of Copenhagen, Copenhagen, Denmark. ¹³Present address: Center for Stem Cell and Regenerative Medicine, Department of Gastroenterology and Hepatology, Tokyo Medical and Dental University (TMDU), Tokyo, Japan. ¹⁴These authors contributed equally: Jordi Guiu, Edouard Hannezo. *e-mail: kim.jensen@bric.ku.dk

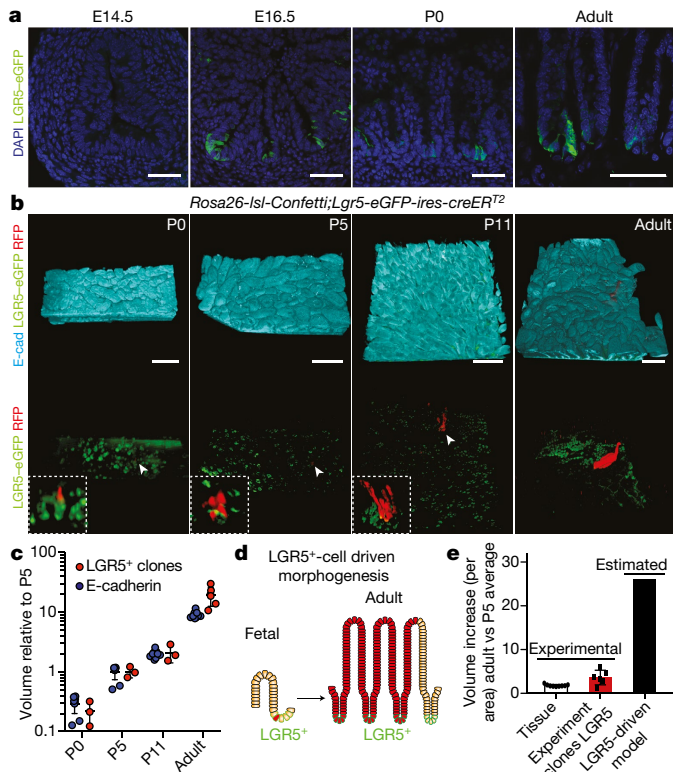


Fig. 1 | Fetal LGR5 progeny contribute to the adult intestinal epithelium, but are insufficient to sustain intestinal growth during development. **a**, Detection of LGR5-eGFP (green) and DAPI (blue) at the indicated time points. Scale bars, 100 μm . Representative images of $n = 3$ biologically independent samples at each time point are shown. **b**, Detection of E-cadherin (E-cad, cyan), GFP (green) and RFP (red) in tissue whole mounts from proximal small intestine isolated from *Rosa26-*Isl1*-Confetti;Lgr5-eGFP-ires-creER^{T2}* mice at P0 ($n = 3$ mice), P5 ($n = 3$ mice), P11 ($n = 3$ mice) and adulthood ($n = 6$ mice) following induction at E16.5 by the administration of 4-hydroxytamoxifen. White arrowheads indicate the clones depicted in the white dashed boxes at higher magnifications. Scale bars, 250 μm . **c**, Relative volume (projected) of clones from **b** and epithelium based on E-cadherin (P0, $n = 9$; P5, $n = 9$; P11, $n = 9$; adult, $n = 9$ mice). Dots indicate independent samples; data are mean \pm s.e.m. **d**, **e**, Model based on LGR5⁺-cell-driven morphogenesis and assessment of the observed and predicted clonal expansion (experiment clones LGR5⁺: P5, $n = 3$; adult, $n = 6$; tissue: P5, $n = 9$; adult, $n = 9$). Data are mean \pm s.e.m.

before P5, and therefore that both P0 and P5 can be used for normalizing clonal persistence (Extended Data Fig. 3l). This strongly suggests that fetal epithelial cells, irrespective of location, contain long-term self-renewal potential and possess the same likelihood of contributing to the adult intestinal stem-cell compartment (Fig. 2e). Of note, although the expansion of the LGR5-targeted clones was slightly higher than that of tissue and KRT19-targeted clones, the difference was small (Fig. 2f). This small difference is likely to reflect a transient proliferative advantage due to their favourable location at the time of induction. Together, these findings indicated that all fetal cells have a similar capacity to contribute to the growth of the intestinal epithelium during development and give rise to adult intestinal stem cells, suggesting that cell fate potential is not fixed in the fetal epithelium.

This finding, however, raised a conundrum, as this implied that cells on villi—which are usually considered as committed to differentiation—contribute substantially in the long term to intestinal growth. Given the influence of gut epithelial geometry on cell fate^{3,15}, we hypothesized that extensive cell rearrangements linked to continuous ‘villification’ could explain this paradox. Between E16.5 and birth, the total number of villi increased approximately sixfold, before reaching the final number characterizing the adult epithelium by P5 (Extended

Data Fig. 4a, b). Therefore, we posited that global 3D epithelial sheet movements during villification could provide a mechanism that enables relocation of villus cells to the proliferative intervillus regions and de novo intervillus formation. Detailed 3D reconstruction of the E16.5 intestine revealed that around 30% of villi presented irregular structures of doublet form, with shared mesenchymal clusters within a specific interval of villus heights (Fig. 3a, Extended Data Fig. 4c–e, Supplementary Videos 3, 4). We speculated that this could be a sign of a single villus undergoing fission. Of note, cells found at the juncture between these structures were LGR5[−] (Extended Data Fig. 4f) and often proliferative (68% of junctures analysed; Fig. 3b, Extended Data Fig. 4g–h, Supplementary Video 5), even though the fission points were distant from the proliferative intervillus regions (Extended Data Fig. 4i). To challenge these observations, we turned to explant cultures, which—despite the intestine not expanding in length—revealed fission events evident from the top of single villi (Fig. 3c, Extended Data Fig. 4j, Supplementary Videos 6, 7). Thus, villi underwent active remodelling, causing pronounced reorganization of the epithelial cell layer.

On the basis of these findings, we turned to a biophysical modelling approach to address whether a minimal model of villus fission could be sufficient to explain the observed long-term equipotency of epithelial cells at E16.5. We modelled both the neutral drift dynamics of proliferative cells restricted to intervillus regions, and the bottom-up influx of cells driving villus elongation, using experimentally derived cell kinetics and geometrical parameters (Supplementary Information ‘Supplementary theory’, Extended Data Fig. 5). Additionally, we incorporated stochastic villus fission (between E16.5 and P4), upon which cells underwent positional changes and a fraction of cells from the parent villus became assigned to the new intervillus region (Fig. 3d). To inform the model, we used the experimentally inferred growth rate of villi number (Extended Data Fig. 6a), so that villus duplication and rapid underlying cell proliferation had a role in fuelling epithelial growth. Within this simplified 2D framework, which takes into account the key features of a more complex 3D process, fission events resulted in the reversible transfer of cells between villus and intervillus regions. We found that, with the experimentally inferred fission rate, just a few days were sufficient to fully erase the positional advantage of progeny from LGR5⁺ cells, resulting in long-term equipotency among all epithelial cells (Fig. 3e–g). In addition to good reproduction of the global evolution of mean clone size, clonal persistence and rootedness (Fig. 3e–g), the model explained several non-trivial aspects of the observed short-term clonal dynamics. In particular, the model predicted that KRT19⁺ clones should initially be larger and more dispersed than LGR5⁺ clones because, even though KRT19⁺ cells were predominantly induced in non-proliferative regions, they participated more readily in villi fission (Extended Data Fig. 6b–e). Furthermore, the model predicted that these KRT19⁺ clones should still be less rooted in intervillus regions than LGR5⁺ clones in the short term (Fig. 3e), with the two converging at later time points. These predictions showed consistently good agreement with the data (detailed statistics in Supplementary Information, ‘Supplementary theory’).

We also performed sensitivity controls on our simulations. First, we assessed the clonal dynamics, only enabling fetal fission from E16.5 to P0. This result showed that fetal remodelling was sufficient to explain the bulk of equipotency between LGR5⁺ and KRT19⁺ clones (Extended Data Fig. 7a–c). By contrast, when the model was applied—either in the absence of de novo villus formation or with villus fission without epithelial reshuffling—a satisfactory fit to the data could not be obtained (Extended Data Fig. 7d–i, Supplementary Information, ‘Supplementary theory’). Moreover, a biophysical model based on the current model for villification, which involves successive rounds of de novo villus formation initiating from the intervillus regions¹⁶, provided a poor fit to the data as this model does not allow the relocation of villus cells to intervillus regions (Extended Data Fig. 7j–o, Supplementary Information, ‘Supplementary theory’). Finally, our biophysical model predicted that the contribution from the KRT19⁺ population should be markedly reduced once villi fission slows down; this was corroborated

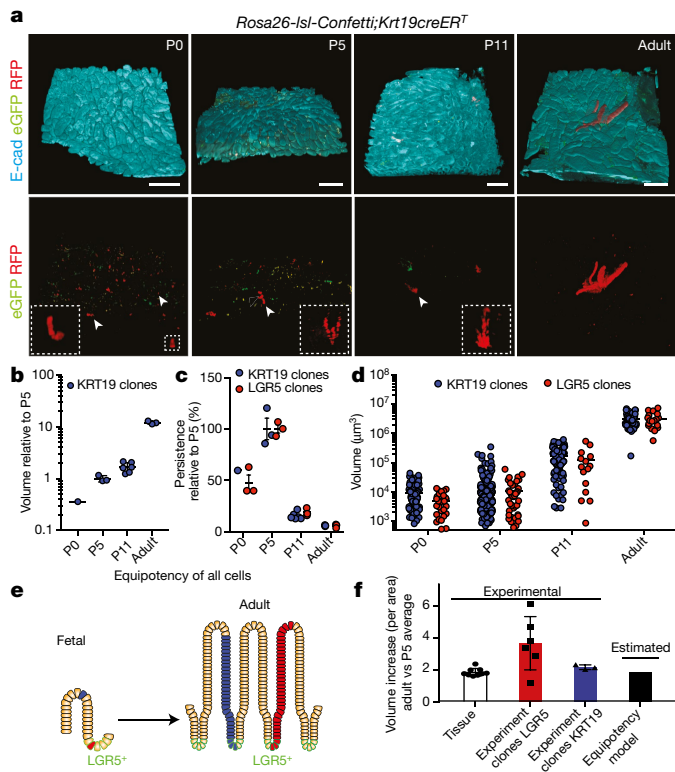


Fig. 2 | Random distribution of intestinal stem cell precursors in the fetal epithelium. **a**, Detection of E-cadherin (cyan), GFP (green) and RFP (red) in tissue whole mounts from proximal small intestine isolated from *Rosa26-lsl-Confetti;Krt19-creER^T* mice at P0 ($n = 1$ mouse), P5 ($n = 3$ mice), P11 ($n = 6$ mice) and adulthood ($n = 3$ mice) following induction at E16.5 by the administration of 4-hydroxytamoxifen. White arrowheads indicate the clones depicted in the white dashed boxes at higher magnifications. Scale bars, 250 μm . **b**, Volume (projected) of clones from the *Krt19-creER^T* induction (from **a**). Each dot represents a mouse. Data are mean \pm s.e.m. **c**, Relative number of clones (projected persistence). Each dot represents an independent biological sample at the indicated time point (from **a** and Fig. 1b). Data are mean \pm s.e.m. **d**, Volume of individual clones (*Krt19-creER^T*: P0, $n = 94$; P5, $n = 244$; P11, $n = 103$; P36 (adult), $n = 42$; *Lgr5-eGFP-ires-creER^{T2}*: P0, $n = 28$; P5, $n = 39$; P11, $n = 15$; adult, $n = 18$). Each dot represents an independent biological sample and the line indicates the mean. **e**, Model based on morphogenesis relying on equipotent stem cells randomly distributed in the tissue. **f**, Assessment of the observed and predicted clonal expansion (experiment clones *Krt19⁺*: P5, $n = 3$; adult, $n = 3$; experiment clones *Lgr5⁺*: P5, $n = 3$; adult, $n = 6$; tissue: P5, $n = 9$; adult, $n = 9$). Data are mean \pm s.e.m.

by fate-mapping experiments starting at P0 rather than E16.5 (Extended Data Fig. 8a–c). This strongly suggested that villus remodelling events are required for recruitment of villus cells to the future stem-cell compartment.

To validate independently that cells specifically located on villi contributed to the adult intestinal epithelium, similarly to *Lgr5⁺*-derived cells, we identified *Krt20* as a marker of fetal and adult villi (Fig. 3h, Extended Data Fig. 9a–c). We observed that 27% of *Krt20⁺* cells scored positive for the proliferation signature, even though these cells were confined to villi. Using a *Krt20*-driven Cre construct, it was evident that labelled cells in the adult epithelium were invariably lost, as reported for other differentiated cell types^{5,6} (Extended Data Fig. 9b). However, in the fetal epithelium, although the majority of labelled cells were initially detected in villi, clones persisted and generated adult intestinal stem cells (Fig. 3i, Extended Data Fig. 9d, Supplementary Information, ‘Supporting clonal data’). Quantitative analysis confirmed the predictions of the model for rootedness, persistence and size of *Krt20* clones, demonstrating once again that intervillus and villus cells display similar behavioural dynamics (Fig. 3j–l). In sum, these findings

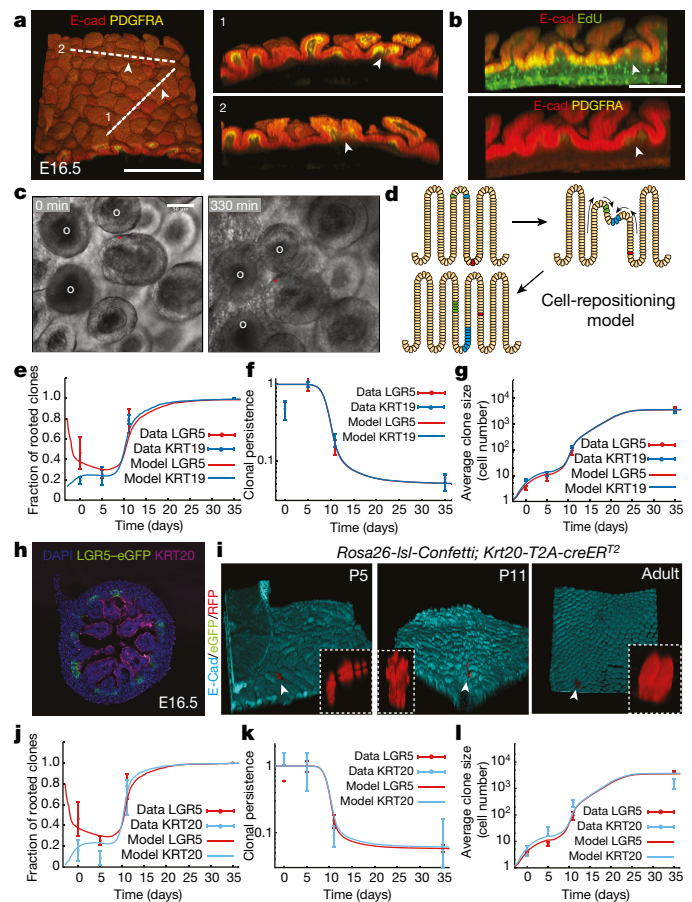


Fig. 3 | Villus fission is required to explain epithelial expansion.

a, Detection of E-cadherin (red) and PDGFRA (yellow) in intestinal whole mount during villus formation. A representative image at E16.5 is shown ($n = 3$ mice). Arrowheads indicate villi with shared mesenchyme. Scale bar, 250 μm . **b**, Labelling with 5-ethynyl-2'-deoxyuridine (EdU, green) and PDGFRA (yellow) and E-cadherin (red) immunofluorescence in intestinal whole mounts following a 1-h EdU pulse at E16.5. Arrowheads indicate proliferative cells at the edge of a putative branching villus ($n = 3$ mice). Scale bar, 100 μm . **c**, Image showing the start and end points from live imaging of a villus undergoing fission (red star) (Supplementary Video 5). White circles indicate reference villi. Three mice were analysed. Scale bar, 50 μm . **d**, Model for cell repositioning based on villi emerging from the intervillus regions or through villus fission. Clones from villi can recolonize the intervillus region and clones from the intervillus region can recolonize villi. **e–g**, Simulation of the clonal dynamics (derived from *Lgr5⁺* and *Krt19⁺* cells) using the cell-repositioning model to predict the fraction of clones (rootedness) rooted in the intervillus region (**e**), clonal persistence (experimental data are also shown in Fig. 2c) (**f**) and mean clone size (**g**). (*Lgr5* data: P0, $n = 3$; P5, $n = 3$; P11, $n = 3$; P36 (adult), $n = 6$ mice; *Krt19* data: P0, $n = 1$; P5, $n = 3$; P11, $n = 6$; adult, $n = 3$ mice). Data are mean \pm s.e.m. **h**, Detection of keratin 20 (*Krt20*, magenta), GFP (*Lgr5-DTR-eGFP*) and DAPI (cyan) at E16.5 in proximal small intestine. A representative image of $n = 3$ independent biological samples is shown. **i**, Detection of E-cadherin (cyan), GFP (green) and RFP (red) in tissue whole mounts from the proximal small intestine isolated from *Rosa26-lsl-Confetti;Krt20-cre-T2A-creER^{T2}* mice at P5 ($n = 4$ mice), P11 ($n = 3$ mice), and adulthood ($n = 5$ mice) following induction at E16.5 by the administration of 4-hydroxytamoxifen. White arrowheads indicate the clones depicted in the white dashed boxes at higher magnifications. **j–l**, Simulation of the clonal dynamics (*Krt20*-derived) using the cell-repositioning model to predict the fraction of clones rooted in the intervillus region (**j**), clonal persistence (experimental data for *Lgr5* are shown in Fig. 2c) (**k**) and mean clone size (**l**). *Lgr5*: P0, $n = 3$; P5, $n = 3$; P11, $n = 3$; adult, $n = 6$ mice analysed; *Krt20*: P0, $n = 3$; P5, $n = 4$; P11, $n = 3$; adult, $n = 5$ mice. Data are mean \pm s.e.m.

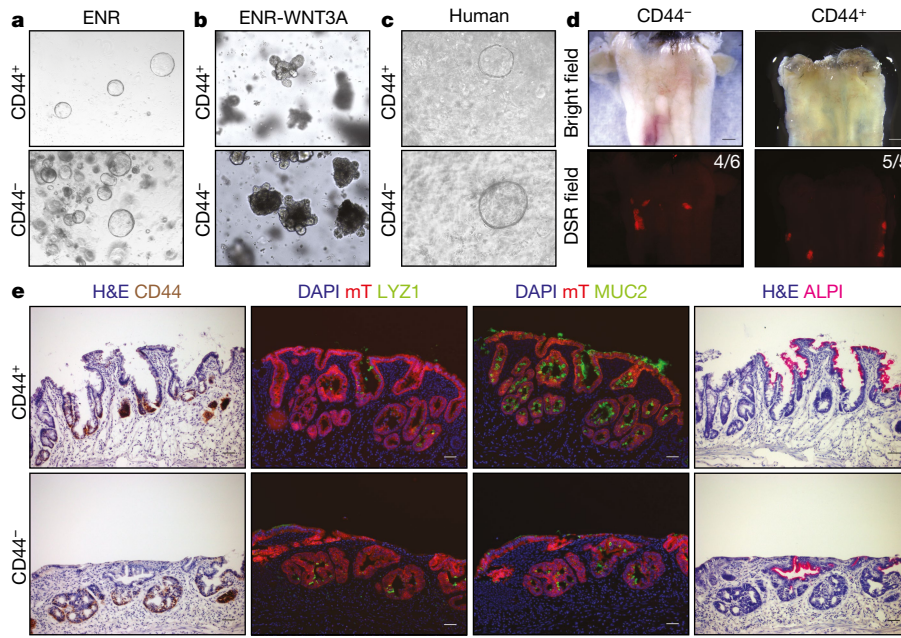


Fig. 4 | Villus and intervillus cells are equipotent and have the same regenerative potential. **a**, Formation of spheroids from DAPI⁻EpCAM⁺CD44⁺ and DAPI⁻EpCAM⁺CD44⁻ epithelial cells isolated from the proximal half of the small intestine of mice at E16.5. A representative image of $n = 3$ independent samples is shown. **b**, Spheroids following treatment with WNT3A. A representative image of $n = 3$ independent samples is shown. **c**, Formation of spheroids from DAPI⁻CD44⁺ and DAPI⁻CD44⁻ epithelial cells isolated from the proximal half of the human fetal small intestine (eight weeks of gestation). A representative picture of $n = 2$ independent samples is shown.

confirmed that the long-term self-renewal potential of intestinal cells becomes sensitive to location soon after birth¹⁷—that is, after major structural changes of villi have ceased and cell migration streams are established.

To further investigate mechanistically the unexpected plasticity of cells from villus (LGR5⁻CD44⁻) and intervillus (LGR5⁺CD44⁺) regions (Extended Data Fig. 10a–d), we took advantage of a 3D culture system that allows cells to self-organize into villus and crypt domains^{18,19}. When sorted from E16.5 proximal small intestine, both populations grew as spheroids, mimicking the immature nature of the fetal small intestine, with comparable plating efficiencies (Fig. 4a, Extended Data Fig. 10e, f). As reported for bulk cultures¹⁹, stimulation with WNT3A was sufficient to convert spheres to budding intestinal organoids, irrespective of their cell-of-origin (Fig. 4b). Notably, CD44⁺ and CD44⁻ cells isolated from intestine in gestational week 8–10 human fetuses were capable of forming spheroids (Fig. 4c). Finally, to challenge the mouse cultures from the two cell populations, the mouse-derived spheroids were transplanted into conditioned mice²⁰ (Extended Data Fig. 10g–j). Again, both cell populations engrafted with similar efficiencies and established CD44⁺ adult stem-cell niches at the bottom of crypts and gave rise to appropriate differentiated lineages including Paneth cells (LYZ1⁺), goblet cells (MUC2⁺) and enterocytes (ALPI⁺) (Fig. 4d, e, Extended Data Fig. 10k). Altogether, these findings demonstrated that fetal villi and intervillus cells had similar potential to grow *in vivo* and *in vitro*, and exhibited the same regenerative potential.

These results of *in vivo* lineage tracing in combination with biophysical modelling and *in vitro* analysis of mouse and human fetal samples demonstrate that fetal intestinal cells—irrespective of their location and marker expression—represent equipotent precursors of adult intestinal stem cells (Extended Data Fig. 10l). We propose that the process of villi fission and tissue bending during intestinal morphogenesis provides a biophysical mechanism to remodel the local microenvironment, allowing cells to switch reversibly between LGR5⁻ and LGR5⁺ states. This behaviour mirrors findings from various adult injury models, in

d, Engraftment of spheroids derived from DAPI⁻EpCAM⁺CD44⁺ and DAPI⁻EpCAM⁺CD44⁻ epithelial cells obtained from E16.5 mT/mG mice. Four out of six mice were successfully engrafted with CD44⁻-derived cells and five out of five mice were engrafted with CD44⁺-derived cells. Scale bars, 10 mm. A representative image of independent engraftments is shown (CD44⁻, $n = 4$; CD44⁺, $n = 5$). **e**, Detection of CD44v6, LYZ1, MUC2 and ALPI in serial section of the engrafted patches (red). Scale bars, 50 μ m. A representative image of independent engraftments is shown (CD44⁻, $n = 4$; CD44⁺, $n = 5$).

which Lgr5⁺ cells lost through damage were subsequently replenished through recolonization by LGR5⁻ cells^{5,6,8,9,21,22}. Notably, the fission mechanism resembled the proposed model for villification in avians, in which longitudinal epithelial ridges generate a zig-zag pattern that breaks up into individual villi¹⁵ and villus geometry was proposed to define gradients of growth factors, thereby establishing distinct cell fates³. We propose that these growth-factor gradients impose specific expression patterns without irreversibly changing cell fates. This is evident from the profound cellular plasticity observed among cells in villi and intervillus regions with respect to their long-term self-renewal potential. This could be a generic property of developmental systems, ensuring the robust coordination of morphogenesis and fate specification²³.

These findings have key implications for the improvement of differentiation protocols to, for example, generate intestinal stem cells from human induced pluripotent stem cells^{24,25}. Consistent with our findings, fetal-like intestinal cells derived from human induced pluripotent stem cells generate cells with characteristics of adult stem cells only upon transplantation^{26–29}. In this sense, the plastic fetal precursor state, which retains the capacity to be induced into an adult stem cell state, represents an attainable target for our strategies to direct differentiation. Understanding how these fetal precursors are induced to become adult stem cells will provide insight into how the process can be orchestrated *in vitro*. As fetal progenitors have been identified in multiple tissues, and all appear to mature in a similar manner upon transplantation^{26–29}, the precursor state is likely to be a general intermediate during tissue maturation. It is therefore tempting to speculate that the plasticity observed during tissue regeneration could be explained via the equipotent progenitor state observed during fetal development.

Online content

Any methods, additional references, Nature Research reporting summaries, source data, statements of data availability and associated accession codes are available at <https://doi.org/10.1038/s41586-019-1212-5>.

Received: 10 December 2017; Accepted: 15 April 2019;
Published online 15 May 2019.

1. Clevers, H. The intestinal crypt, a prototype stem cell compartment. *Cell* **154**, 274–284 (2013).
2. Barker, N. et al. Identification of stem cells in small intestine and colon by marker gene *Lgr5*. *Nature* **449**, 1003–1007 (2007).
3. Shyer, A. E., Huycke, T. R., Lee, C., Mahadevan, L. & Tabin, C. J. Bending gradients: how the intestinal stem cell gets its home. *Cell* **161**, 569–580 (2015).
4. Nigmatullina, L. et al. *Id2* controls specification of *Lgr5*⁺ intestinal stem cell progenitors during gut development. *EMBO J.* **36**, 869–885 (2017).
5. Tetteh, P. W. et al. Replacement of lost *Lgr5*-positive stem cells through plasticity of their enterocyte-lineage daughters. *Cell Stem Cell* **18**, 203–213 (2016).
6. van Es, J. H. et al. *Dll1*⁺ secretory progenitor cells revert to stem cells upon crypt damage. *Nat. Cell Biol.* **14**, 1099–1104 (2012).
7. Buczaccki, S. J. et al. Intestinal label-retaining cells are secretory precursors expressing *Lgr5*. *Nature* **495**, 65–69 (2013).
8. Yui, S. et al. YAP/TAZ-dependent reprogramming of colonic epithelium links ECM remodeling to tissue regeneration. *Cell Stem Cell* **22**, 35–49 (2018).
9. Nusse, Y. M. et al. Parasitic helminths induce fetal-like reversion in the intestinal stem cell niche. *Nature* **559**, 109–113 (2018).
10. Guiu, J. & Jensen, K. B. From definitive endoderm to gut: a process of growth and maturation. *Stem Cells Dev.* **24**, 1972–1983 (2015).
11. Sumigray, K. D., Terwilliger, M. & Lechler, T. Morphogenesis and compartmentalization of the intestinal crypt. *Dev. Cell* **45**, 183–197 (2018).
12. Mustata, R. C. et al. Identification of *Lgr5*-independent spheroid-generating progenitors of the mouse fetal intestinal epithelium. *Cell Reports* **5**, 421–432 (2013).
13. Moor, A. E. et al. Spatial reconstruction of single enterocytes uncovers broad zonation along the intestinal villus axis. *Cell* **175**, 1156–1167 (2018).
14. Merlos-Suarez, A. et al. The intestinal stem cell signature identifies colorectal cancer stem cells and predicts disease relapse. *Cell Stem Cell* **8**, 511–524 (2011).
15. Shyer, A. E. et al. Villification: how the gut gets its villi. *Science* **342**, 212–218 (2013).
16. Walton, K. D. et al. Hedgehog-responsive mesenchymal clusters direct patterning and emergence of intestinal villi. *Proc. Natl Acad. Sci. USA* **109**, 15817–15822 (2012).
17. Itzkovitz, S., Blat, I. C., Jacks, T., Clevers, H. & van Oudenaarden, A. Optimality in the development of intestinal crypts. *Cell* **148**, 608–619 (2012).
18. Sato, T. et al. Single *Lgr5* stem cells build crypt–villus structures in vitro without a mesenchymal niche. *Nature* **459**, 262–265 (2009).
19. Fordham, R. P. et al. Transplantation of expanded fetal intestinal progenitors contributes to colon regeneration after injury. *Cell Stem Cell* **13**, 734–744 (2013).
20. Yui, S. et al. Functional engraftment of colon epithelium expanded in vitro from a single adult *Lgr5*⁺ stem cell. *Nat. Med.* **18**, 618–623 (2012).
21. Ritsma, L. et al. Intestinal crypt homeostasis revealed at single-stem-cell level by *in vivo* live imaging. *Nature* **507**, 362–365 (2014).
22. Tian, H. et al. A reserve stem cell population in small intestine renders *Lgr5*-positive cells dispensable. *Nature* **478**, 255–259 (2011).
23. Chan, C. J., Heisenberg, C. P. & Hiriagi, T. Coordination of morphogenesis and cell-fate specification in development. *Curr. Biol.* **27**, R1024–R1035 (2017).
24. Hannan, N. R. et al. Generation of multipotent foregut stem cells from human pluripotent stem cells. *Stem Cell Reports* **1**, 293–306 (2013).
25. Spence, J. R. et al. Directed differentiation of human pluripotent stem cells into intestinal tissue *in vitro*. *Nature* **470**, 105–109 (2011).
26. Watson, C. L. et al. An *in vivo* model of human small intestine using pluripotent stem cells. *Nat. Med.* **20**, 1310–1314 (2014).
27. Sun, X. et al. Directed differentiation of human embryonic stem cells into thymic epithelial progenitor-like cells reconstitutes the thymic microenvironment *in vivo*. *Cell Stem Cell* **13**, 230–236 (2013).
28. McCracken, K. W. et al. Modelling human development and disease in pluripotent stem-cell-derived gastric organoids. *Nature* **516**, 400–404 (2014).
29. Kroon, E. et al. Pancreatic endoderm derived from human embryonic stem cells generates glucose-responsive insulin-secreting cells *in vivo*. *Nat. Biotechnol.* **26**, 443–452 (2008).

Acknowledgements We thank members of the Jensen and Simons laboratories for comments and suggestion; H. Clevers (*Rosa26-Isi-Confetti* and *Lgr5-eGFP-ires-creER^{T2}*), F. de Sauvage (Genentech) (*Lgr5-iDTR-eGFP*), A. McMahon (*Krt20-T2A-creER^{T2}*) and G. Gu (*Krt19-creER¹*) for gifts of mice; and Y. Antoku in Imaging core facilities at BRIC and the Center for Advanced Bioimaging at University of Copenhagen for experimental support. This work was supported by Lundbeck Foundation (R105-A9755 to K.B.J.; R190-2014-3904 to T.H.P.), the Novo Nordisk Foundation (NNF14OC0012927 to K.B.J. and NNF16OC0019920 to K.K.), the Carlsberg Foundation, EMBO Young Investigator programme (to K.B.J.), the Marie Curie fellowship programme (S.Y. and J.G.; 625238/FP7-PEOPLE-2013-IF, 656099/H2020-MSCA-IF-2014) and the Wellcome Trust (098357/Z/12/Z to B.D.S., 110326/Z/15/Z to E.H.). B.D.S. also acknowledges funding from the Royal Society E. P. Abraham Research Professorship (RP\R1\180165). This project has received funding from the European Union's Horizon 2020 research and innovation programme (grant agreements STEMHEALTH ERCCoG682665 and INTENS 668294 to K.B.J.). The Novo Nordisk Foundation Center for Stem Cell Biology and the Novo Nordisk Foundation Center for Basic Metabolic Research are supported by Novo Nordisk Foundation grants (NNF17CC0027852 and NNF18CC0034900, respectively).

Reviewer information *Nature* thanks Hans Clevers, Fred de Sauvage and the other anonymous reviewer(s) for their contribution to the peer review of this work.

Author contributions J.G. and K.B.J. conceived the project. J.G., E.H., B.D.S. and K.B.J. designed experiments. J.G., S.Y., S.U. and M.M. performed experiments. A.J., S.P., L.L., L.S.M., C.Y.A., L.L.T., K.J.H., A.L. and R.H.O. collected and processed human fetal material. S.D., T.H.P. and K.K. analysed single-cell sequencing data. E.H. and B.D.S. designed and performed the mathematical modelling. J.G. wrote the manuscript with input from K.B.J., E.H. and B.D.S. J.G., S.Y., B.D.S. and K.B.J. acquired funding. B.D.S. and K.B.J. supervised the project.

Competing interests The authors declare no competing interests.

Additional information

Extended data is available for this paper at <https://doi.org/10.1038/s41586-019-1212-5>.

Supplementary information is available for this paper at <https://doi.org/10.1038/s41586-019-1212-5>.

Reprints and permissions information is available at <http://www.nature.com/reprints>.

Correspondence and requests for materials should be addressed to K.B.J.
Publisher's note: Springer Nature remains neutral with regard to jurisdictional claims in published maps and institutional affiliations.

© The Author(s), under exclusive licence to Springer Nature Limited 2019

METHODS

Mice. Unless otherwise specified, C57BL/6J mice (purchased from Taconic) were used for all the experiments. Transgenic murine lines used in the experiments have been previously described: *Rosa26-mT/mG* (ref. ³⁰), *Lgr5-eGFP-ires-creER^{T2}* (ref. ²), *Krt19-creER^T* (ref. ³¹), *RAG2^{-/-}* (Taconic), *Rosa26-lsl-Confetti* (ref. ³²), *Lgr5-DTR-eGFP* (ref. ²²), *Villin-cre³³*, *Krt20-T2A-creER^{T2}* (Jackson laboratories, stock no. 030600), and *Rosa26-lsl-tdTomato³⁴*. CD1 mice (Janvier) were used as foster mothers in the lineage-tracing experiments.

None of the animals used in these studies had been subjected to prior procedures and were drug- and test-naïve. All animals were housed in specific-pathogen-free animal facilities, in either open or individually ventilated cages always with companion mice, and cages were placed under a 12-h light–dark cycle. Food and water were provided ad libitum. Randomized cohorts including both male and female animals were distributed in an unblinded manner into the experimental time points for analysis. Sample sizes were selected to provide sufficient statistical power for analysis. The National Animal Ethics Committee in Denmark reviewed and approved all animal procedures (Permit numbers 2013-15-2934-00756 and 2013-15-2934-00927).

Lineage-tracing experiments and quantification. Pregnant females carrying embryos at E16.5 were intraperitoneally injected with the indicated amount of 4-hydroxytamoxifen (4OHT, Sigma) and progesterone (50 µg, Sigma) in corn oil (Sigma). Pregnant *Lgr5-eGFP-ires-creER^{T2}* and *Krt20-T2A-creER^{T2}* mice were injected with 1 mg 4OHT; pregnant *Krt19-creER^{T2}* mice were injected with 100 µg 4OHT. Pregnant *Krt19-creER^T;Rosa26^{mT/mG}* mice were injected with 1 mg 4OHT. Newborn *Krt19-creER^T;Rosa26-lsl-Confetti* and *Lgr5-eGFP-ires-creER^{T2};Rosa26-lsl-Confetti* P0 mice were injected with 10 µg 4OHT. *Lgr5-eGFP-ires-creER^{T2}* mice were delivered by caesarean section at E18.5 and newborns were transferred to CD1 foster mothers. The proximal half of the small intestine was collected at the time points indicated in the figures. In *Krt19-creER^T;Rosa26-lsl-Confetti* and *Lgr5-eGFP-ires-creER^{T2};Rosa26-lsl-Confetti* quantifications, only red clones were considered; for *Krt20-T2A-creER^{T2}*, red and YFP clones were considered. The projections of volume, number of villi and number of clones (persistence) at the indicated time points were calculated by multiplying the volume/unit area, number of villi/unit area and number of clones/unit area by the total surface area of the proximal half of the intestine at each time point analysed.

Transplantation. Transplantation was performed using *RAG2^{-/-}* mice as recipients, essentially as previously described²⁰. In brief, colitis was induced in *RAG2^{-/-}* mice (3–6 months old) by administration of 3.3% DSS (MP Biomedicals; molecular mass 36,000–50,000) in the drinking water for 5 days followed by normal water. Mice were subsequently infused with cultured intestinal epithelial cells derived from *Rosa26^{mT/mG}* mice on day 8 and day 11 after the beginning of DSS treatment. Cells were cultured in Matrigel as described below. At passage 5, epithelial cells were released from matrix, and mechanically dissociated into epithelial sheets. After washing, cell fragments from approximately 600 organoids were resuspended in 300 µl 5% Matrigel in PBS. Under general anaesthesia (isoflurane; Piramal Healthcare), a flexible catheter was inserted into the colon of mice and the cell suspension was subsequently infused slowly into the colonic lumen. The anus was sealed with surgical histoacryl glue (B. Braun) for 3 h to reduce flow in the colon. The animals were carefully monitored during the colitis and following transplantation. Two weeks after the second transplantation, recipient mice were killed and colons were collected and processed for analysis.

Human fetal samples. Human fetal tissue collection was approved by the regional ethics committee (permit number H-1-2012-007 and 258206). The adult patients gave their informed written and oral consent. None of the terminations were for reasons of fetal abnormality and the fetal tissue was available following elective termination of pregnancy during first trimester.

Imaging and histology. *Whole-mount immunostaining.* The proximal half of the small intestine was fixed with 4% paraformaldehyde (PFA) from 3 h to overnight at 4 °C. The samples were then dissected into smaller fragments (approximately 4 mm × 4 mm) followed by dehydration in methanol. Samples were stored in methanol at –20 °C. Then, the tissue was rehydrated in a PBS series before staining with all steps being performed at 4 °C. In brief, samples were blocked and permeabilized in 1% bovine serum albumin (Sigma), 0.5% Triton X-100 (Triton X-100 Surfact-Amps Detergent Solution, Thermo Fisher) in PBS for 24 h. Primary antibodies (indicated in Supplementary Table 1) were incubated in 1% bovine serum albumin (Sigma), 0.5% Triton X-100 in PBS for 48 h. Tissue was subsequently washed in 0.5% Triton X-100 in PBS overnight. Secondary antibodies (indicated in Supplementary Table 1) were incubated in 1% bovine serum albumin (Sigma), 0.5% Triton X-100 in PBS for 48 h and the tissue was subsequently washed overnight with 0.5% Triton X-100 in PBS. Diamidino-2-phenylindole dihydrochloride (DAPI; 1 µM; Sigma) was used to counterstain nuclei in the indicated experiments. Samples were then dehydrated in methanol and kept at –20 °C. Samples were cleared using 1:2 benzyl alcohol:benzyl benzoate (BABB) (Sigma). In brief, 5 changes (1 min each) of BABB:methanol 1:1, then 5 changes (2 min each) of BABB. The samples were

subsequently mounted within a Fast well (FW20-FastWells 20-mm diameter × 1.0-mm depth or 25 × 25 mm, Grace-Biolabs). Z-stack images were acquired using laser-scanning confocal microscopy (Leica TSC SP8). Three-dimensional reconstructions were done using Fiji software and clone volume was assessed using Velocity v.6.3.0 (Perkin Elmer).

EdU staining. Mice were intraperitoneally injected with EdU (pregnant females carrying embryos at E16.5 with 250 µg; P0 with 25 µg; P5 with 31.25 µg, P11 with 37.5 µg and adult with 250 µg) and processed according to the manufacturer's instructions (Click-iT Plus EdU Alexa Fluor 488 Flow Cytometry Assay Kit or Click-iT EdU Alexa Fluor 555 Imaging Kit, Thermo Fisher). Following a 1-h chase, the tissue was processed as described in the previous section. Before (2D staining) or after (whole-mount immunostaining) primary and secondary antibody staining, EdU was developed using Click-iT technology. DAPI (1 µM; Sigma) was used to counterstain nuclei in the indicated experiments.

Two-dimensional immunostaining. Proximal halves of the small intestine were fixed with 4% PFA from 3 h to overnight at 4 °C and following dehydration, embedded in paraffin. Sections (5–8-µm thick) were prepared with a microtome.

The luminal perimeter was measured at the indicated time points in sections of small intestines stained with Haematoxylin QS (Vector) and Eosin Solution Aqueous (Sigma). Alkaline phosphatase staining was performed using Vector Red Substrate Kit (Vector). Images were acquired using NDP Zoomer Digital Pathology (Hamamatsu) and subsequently analysed in NDP.view2 software.

To perform immunohistochemistry and immunofluorescence on paraffin-embedded tissues, sections were rehydrated before antigen retrieval. Diva Decloaker solution (Biocare Medical) and Retriever 2100 (Aptum) were used at this step. Then, blocking and permeabilization was performed in 10% adult bovine serum (Sigma), 0.3% Triton X-100 in PBS for at least 1 h at room temperature. Primary antibodies (indicated in Supplementary Table 1) were incubated overnight in 10% adult bovine serum (Sigma) at 4 °C. Secondary antibodies (indicated in Supplementary Table 1) were incubated for 1–2 h at room temperature in 0.5% bovine serum albumin (Sigma) or in the ready-to-use solutions (Vector), when using horseradish peroxidase-conjugated secondary antibodies. For immunofluorescence, DAPI (1 µM; Sigma) was used to counterstain nuclei in the indicated experiments. For immunofluorescence, Alexa-Fluor-conjugated secondary antibodies were used (detailed in Supplementary Table 1), except with anti-CD44 antibody (indicated in Supplementary Table 1), when TSA Plus Cyanine 3 and Fluorescein System (Perkin Elmer) was used. For immunohistochemistry, secondary antibodies were developed using DAB (ImmPACT DAB Peroxidase (HRP) Substrate, Vector) and nuclei were subsequently visualized with Haematoxylin QS (Vector). Fluorescent images were acquired using laser-scanning confocal microscopes (Leica TSC SP8), images of engrafted patches were acquired using a Zeiss Imager M2 microscope equipped with ORCA-R² Digital CCD camera C10600 (Hamamatsu), and immunohistochemistry samples were imaged using NDP Zoomer Digital Pathology (Hamamatsu). All images were subsequently analysed in NDP.view2 software, Fiji and Adobe Photoshop CS6.

Sequential sectioning of grafted epithelial patches. Two weeks after the second transplantation, recipient *RAG2^{-/-}* mice were killed by cervical dislocation and colons were dissected. After washing with PBS, colons were opened longitudinally and imaged by stereomicroscopy (Leica M165FC). Engrafted patches were dissected from the colon and fixed with 4% PFA for 3 h followed by incubation in 20% sucrose solution in PBS overnight. Tissue fragments were embedded in OCT. Eight-micrometre sequential frozen sections were analysed histologically as described above.

Intestinal live imaging of explant cultures. The proximal half of small intestine was isolated from E16.5 embryos. The intestine was subsequently cut open longitudinally and attached from both ends of the intestine to a glass-bottomed plate using surgical histoacryl glue (B. Braun). Explant cultures were covered in BGJb Medium (Thermo Fisher Scientific) supplemented with 0.1 mg/ml ascorbic acid (Sigma) and 1% penicillin–streptomycin (Life technologies, GIBCO) as previously described³⁵. Samples were imaged using a Delta Vision deconvolution microscope (GE Healthcare) and Widefield Zeiss AxioImager microscope.

Isolation of epithelial cells from the fetal epithelium and purification by flow cytometry. Fetal small intestine from mouse or human fetuses was dissected and incubated with collagenase solution (125 µg/ml in PBS) for 45 min at 37 °C and subjected to vigorous pipetting every 15 min using a P1000 pipette. Released cells were pelleted and resuspended in PBS supplemented with 1% BSA and incubated with fluorescent-conjugated primary antibodies (indicated in Supplementary Table 1) for 30 min on ice. After washing, DAPI (Sigma; 1 µM) was added to the cell suspension to facilitate exclusion of dead cells by flow cytometry. Purified cell populations were subsequently isolated using a FACSAria I or III (BD Bioscience). After isolation, cells were embedded in growth factor reduced Matrigel (Corning) in the presence of human EGF (Peprotech; 50 ng/ml), murine noggin (Peprotech; 100 ng/ml), human noggin (Peprotech; 100 ng/ml), mouse R-spondin1 (R&D Systems; 500 ng/ml) as previously reported²⁰. In some experiments Wnt3a-

conditioned medium (50% in volume) was added as a supplement as indicated. Prostaglandin E2 (2.5 μ M, Sigma) was added to the human fetal cultures. In all experiments using mouse organoids, cells were collected from wild-type C57/BL6 mice (Taconic). Cells were cultured in a dome-shaped 25- μ l extracellular matrix droplet and 250 μ l culture medium was added to each well in a 48-well plate (flat bottom; Corning). Medium was subsequently changed every 2–3 days. For human samples we observed no discernable effect of whether the pregnant mother was a smoker or not.

Single-cell sequencing. Cells were isolated from a pool of six proximal small intestines (1 cm in length each) at E16.5 using collagenase treatment and cell sorting as described in the previous section. DAPI⁻CD31⁻CD45⁻EpCAM⁺ cells (20,000 cells) were processed using 10x Genomics Chromium protocols (version 2 chemistry).

RNA-sequencing data analysis. Reads were de-multiplexed, aligned and counted using the 10x Genomics Cellranger v.2.1.0 software³⁶. The refdata-cellranger-mm10-1.2.0 reference was downloaded from the 10x Genomics website (<https://support.10xgenomics.com/>). The resulting filtered count matrix was loaded into Pagoda 2 (ref. ³⁷) for data exploration and Seurat 2.3 (ref. ³⁸) for visualization purposes. Genes that were expressed in fewer than 5 cells were removed. Cells expressing less than 200 genes, more than 6,000 genes or more than 10% mitochondrial genes were removed. Before filtering, the dataset consisted of 3,770 cells. After quality control, 3,509 cells remained.

Scores for signatures for adult epithelium single-cell zones 1–5 and the proliferation signature were calculated using Seurat's AddModuleScore function. The corresponding gene lists were extracted from Supplementary Table 1^{14,15}.

Cells were considered as positive for a particular zone signature¹³ when their expression was higher than mean + 1 s.d. for that particular signature. Cells were considered as positive for the proliferation signature when their scores were >0 in Seurat 2.3's normalized expression value. Similarly, cells were considered as positive for individual genes when their scores were >0 in Seurat's normalized expression value.

Statistics. The number of biological and technical replicates and the number of animals are indicated in figure legends and text. All tested animals were included. Sample size was not predetermined. For all experiments with error bars, the s.e.m. or s.d. was calculated to indicate the variation within each experiment or

sample. Statistical *t*-tests were used to assess significance in the indicated experiments.

Reporting summary. Further information on research design is available in the Nature Research Reporting Summary linked to this paper.

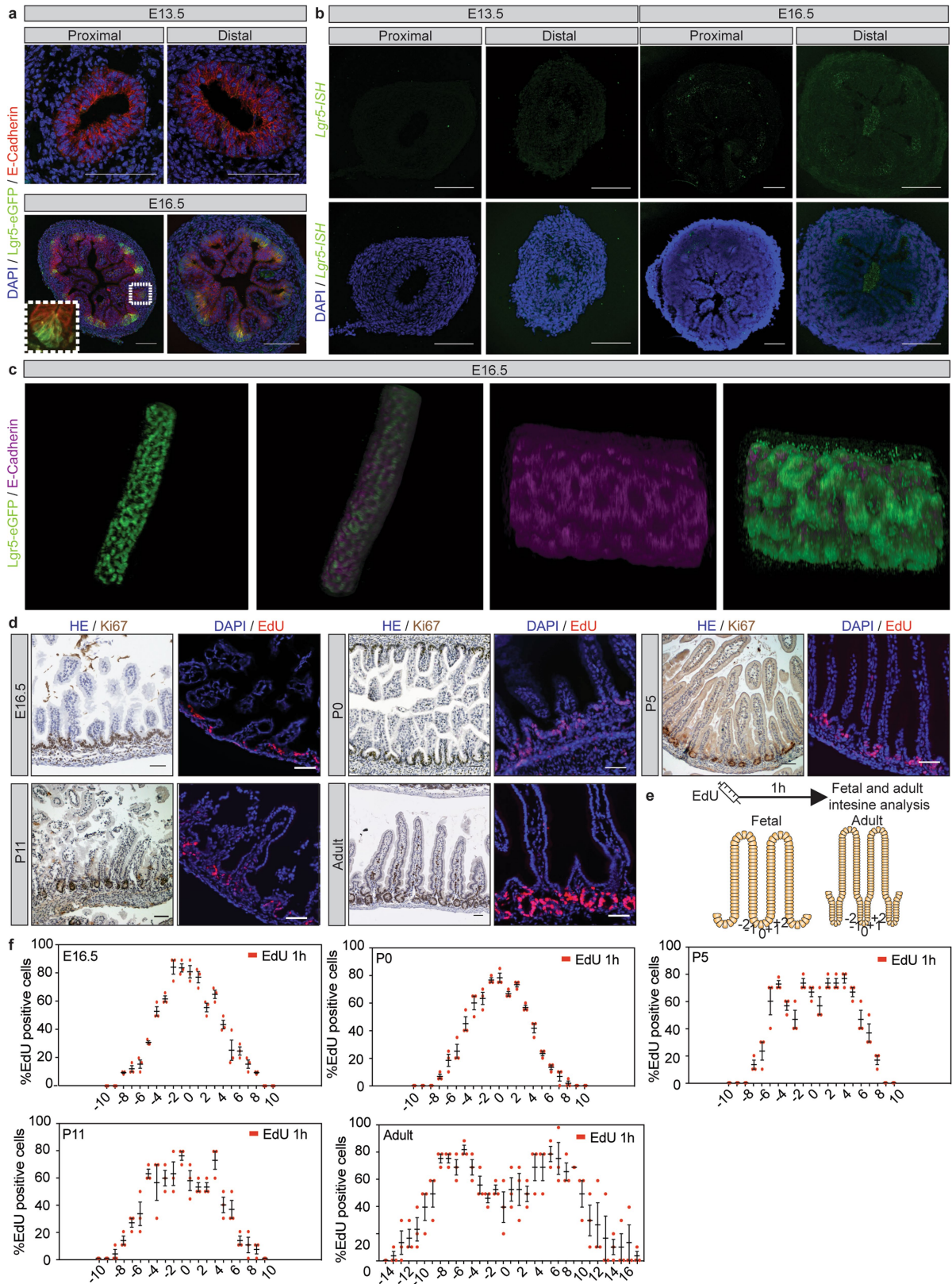
Data availability

RNA sequencing data that support the findings of this study have been deposited in the ArrayExpress database at EMBL-EBI (www.ebi.ac.uk/arrayexpress) under accession number E-MTAB-7660. Raw data used are provided in the Source Data files. All other data supporting the findings of this study are available from the corresponding author on reasonable request.

Code availability

Code for the biophysical modelling is provided as a Supplementary Information file.

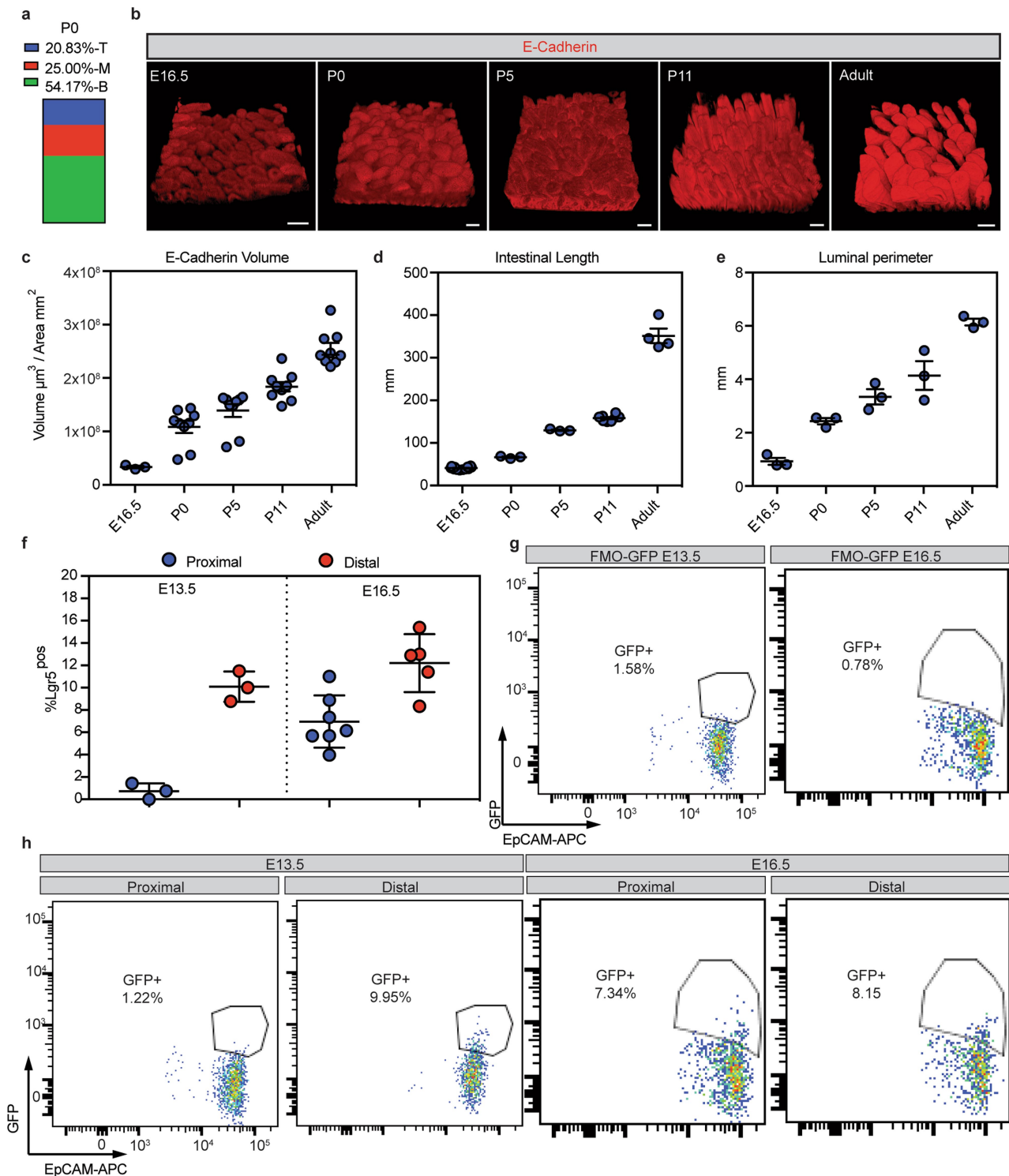
30. Muzumdar, M. D., Tasic, B., Miyamichi, K., Li, L. & Luo, L. A global double-fluorescent Cre reporter mouse. *Genesis* **45**, 593–605 (2007).
31. Means, A. L., Xu, Y., Zhao, A., Ray, K. C. & Gu, G. A CK19^{CreERT} knockin mouse line allows for conditional DNA recombination in epithelial cells in multiple endodermal organs. *Genesis* **46**, 318–323 (2008).
32. Snippert, H. J. et al. Intestinal crypt homeostasis results from neutral competition between symmetrically dividing Lgr5 stem cells. *Cell* **143**, 134–144 (2010).
33. el Marjou, F. et al. Tissue-specific and inducible Cre-mediated recombination in the gut epithelium. *Genesis* **39**, 186–193 (2004).
34. Madisen, L. et al. A robust and high-throughput Cre reporting and characterization system for the whole mouse brain. *Nat. Neurosci.* **13**, 133–140 (2010).
35. Walton, K. D. & Kolterud, A. Mouse fetal whole intestine culture system for *ex vivo* manipulation of signaling pathways and three-dimensional live imaging of villus development. *J. Vis. Exp.* **91**, e51817 (2014).
36. Zheng, G. X. et al. Massively parallel digital transcriptional profiling of single cells. *Nat. Commun.* **8**, 14049 (2017).
37. Fan, J. et al. Characterizing transcriptional heterogeneity through pathway and gene set overdispersion analysis. *Nat. Methods* **13**, 241–244 (2016).
38. Butler, A., Hoffman, P., Smibert, P., Papalexi, E. & Satija, R. Integrating single-cell transcriptomic data across different conditions, technologies, and species. *Nat. Biotechnol.* **36**, 411–420 (2018).



Extended Data Fig. 1 | See next page for caption.

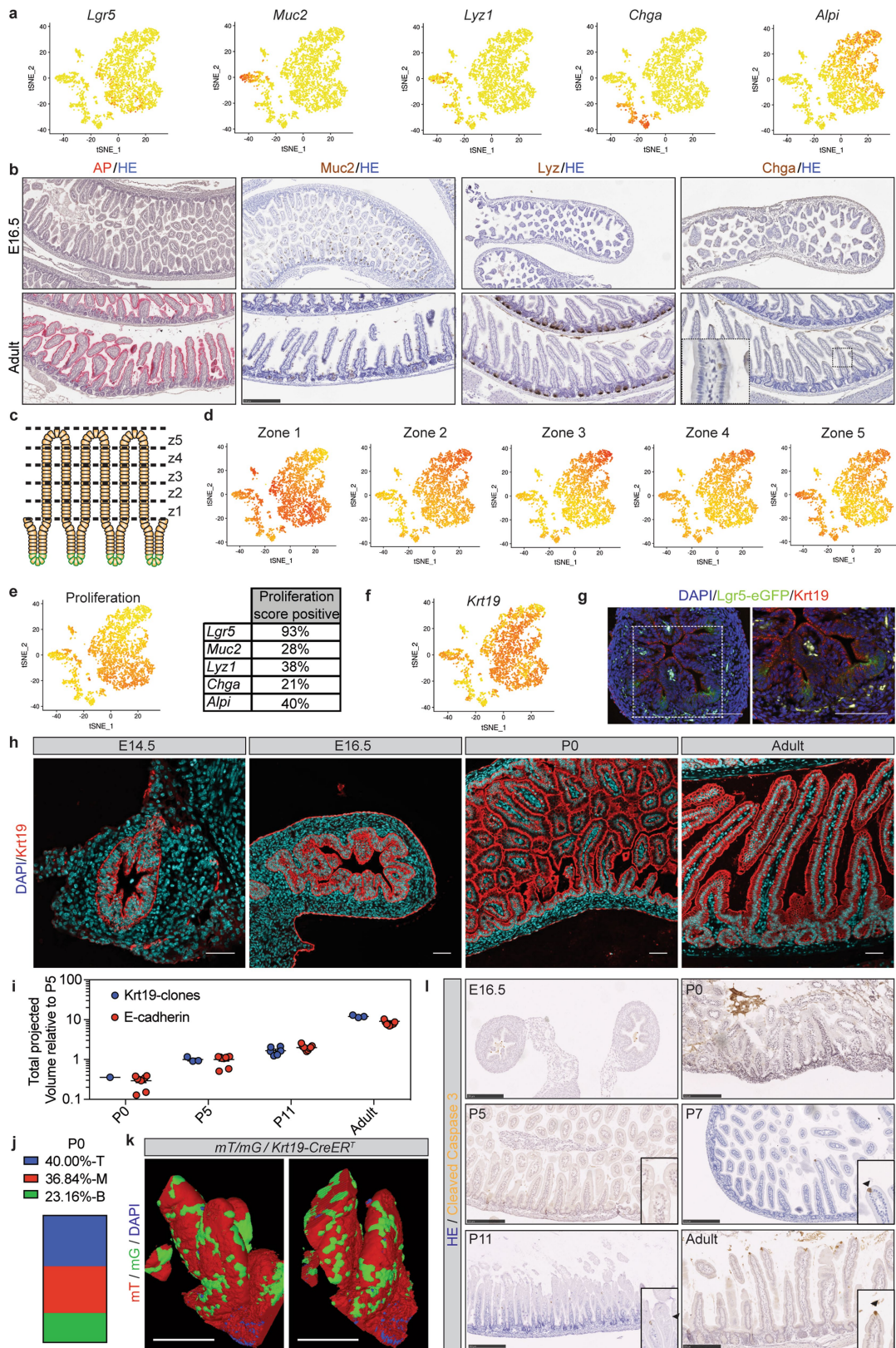
Extended Data Fig. 1 | LGR5⁺ cells and proliferative cells are restricted to the intervillus regions. **a**, Detection of E-cadherin (red) and GFP (*Lgr5-DTR-eGFP*) at E13.5 and E16.5 in proximal and distal small intestine. Tissue is counterstained with DAPI (cyan). A representative image from each time point and intestinal segment is shown ($n = 3$ mice analysed). **b**, In situ hybridization of endogenous *Lgr5* at E13.5 and E16.5 in proximal and distal small intestine. Tissue is counterstained with DAPI (cyan). A representative image from each time point and intestinal segment is shown ($n = 3$ mice analysed). **c**, Detection of E-cadherin (magenta) and GFP (*Lgr5-DTR-eGFP*) in intestinal whole

mount at E16.5 in proximal small intestine. A representative image from $n = 3$ independent samples is shown. **d**, Detection of Ki67 and EdU (red) following a 1-h pulse at the indicated time points (left and right, respectively). Three mice were analysed at each time point and a representative image is shown. Scale bars, 50 μm . **e**, **f**, Quantification of number and location of EdU⁺ cells as depicted (**e**) from at least ten intervillus regions per mouse at E16.5, P5, P11 and adult, and 20 intervillus regions per mouse at P0 up to position 10 and position 17 (adult). Samples from three mice were analysed at each time point. Data are mean \pm s.e.m.



Extended Data Fig. 2 | LGR5-derived clones are located in intervillus regions and qualitative and quantitative morphological analysis of the intestine from fetal to adult stages. **a**, Quantification of localization of labelled clones at P0 following labelling at E16.5 in *Rosa26-IsI-Confetti;Lgr5-eGFP-ires-creER^{T2}* mice. Villi containing clones were divided into three equal regions (T, top; M, middle; B, bottom) based on the *z* projections in 3D to determine the clone localization at P0 ($n = 24$ clones). **b**, Detection of E-cadherin (red) in whole mounts at the indicated time points. Scale bars, 100 μm . A minimum of three mice were analysed at each time point and representative images are shown (E16.5 $n = 3$, P0 $n = 9$, P5 $n = 9$, P11 $n = 9$, adult $n = 9$ mice). **c**, Measurements of the total epithelial volume per unit area based on detection of E-cadherin relative to the area of the intestine (samples from **b**). Dots represent

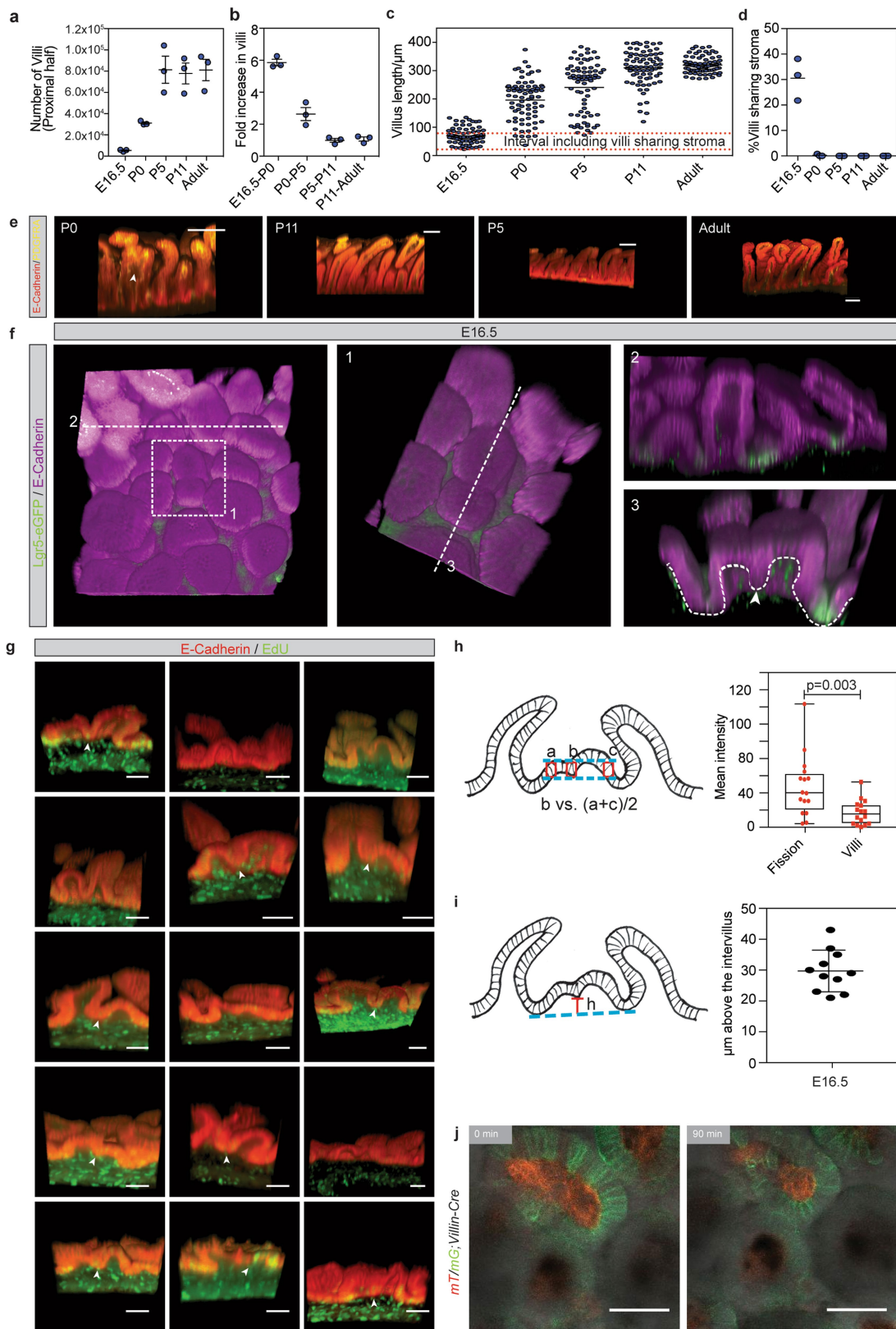
independent biological samples; data are mean \pm s.e.m. **d**, Length of the small intestine at E16.5 ($n = 12$), P0 ($n = 3$), P5 ($n = 3$), P11 ($n = 8$) and adult ($n = 4$). Dots represent individual mice and lines represent the mean \pm s.e.m. **e**, Luminal perimeter of the small intestine at E16.5, P0, P5, P11 and adult. Dots represent individual mice ($n = 3$) and lines represent the mean \pm s.e.m. **f-h**, Quantification of GFP as a proxy for LGR5 in proximal and distal small intestine at E13.5 ($n = 3$ mice both proximal and distal) and E16.5 ($n = 7$ mice proximal, $n = 5$ mice distal) small intestines (**f**). **g**, Fluorescence minus one (FMO) controls used to establish the positive gates. **h**, Representative FACS dot plot illustrating the gating strategy to quantify the size of the LGR5-DTR-eGFP⁺ population (gate, DAPI⁻CD31⁻CD45⁻EpCAM⁺). Dots represent measurement in individual mice; data are mean \pm s.e.m.



Extended Data Fig. 3 | See next page for caption.

Extended Data Fig. 3 | Characterization of the fetal small intestinal epithelium. **a**, *t*-distributed stochastic neighbor embedding (*t*-SNE) plots from scRNA-seq of epithelial cells from the proximal small intestine showing expression of intestinal stem-cell (*Lgr5*) and differentiation markers (*Muc2*, *Lyz1*, *ChgA* and *Alpi*). Darker colour indicates higher normalized gene expression. Each dot represents a cell; a total of 3,509 cells is shown. **b**, Detection of differentiation markers in E16.5 and adult small intestine. Tissue is counterstained with haematoxylin and eosin. Scale bar, 250 μ m. Samples from $n = 3$ mice were analysed at each time point and representative images are shown. **c**, Cartoon depicting that adult villi are transcriptionally zoned in five regions numbered from bottom to top (z , zone). **d**, *t*-SNE plots showing enrichment of villi clusters in the scRNA-seq from E16.5 small intestine. **e**, *t*-SNE plot showing the enrichment of a proliferation signature in specific cell populations (left) and fraction of cells in each subpopulation scoring positive for the proliferation gene signature (right). A darker colour in the *t*-SNE plot indicates higher expression levels of the proliferation gene signature. **f**, *t*-SNE plot showing expression of keratin 19 (*Krt19*). Darker colour indicates higher normalized gene expression levels. **g**, Detection of KRT19 (red) and GFP (*Lgr5-DTR-eGFP*) at E16.5 in proximal small intestine. Tissue is counterstained with DAPI (cyan). Scale bars, 50 μ m. Samples

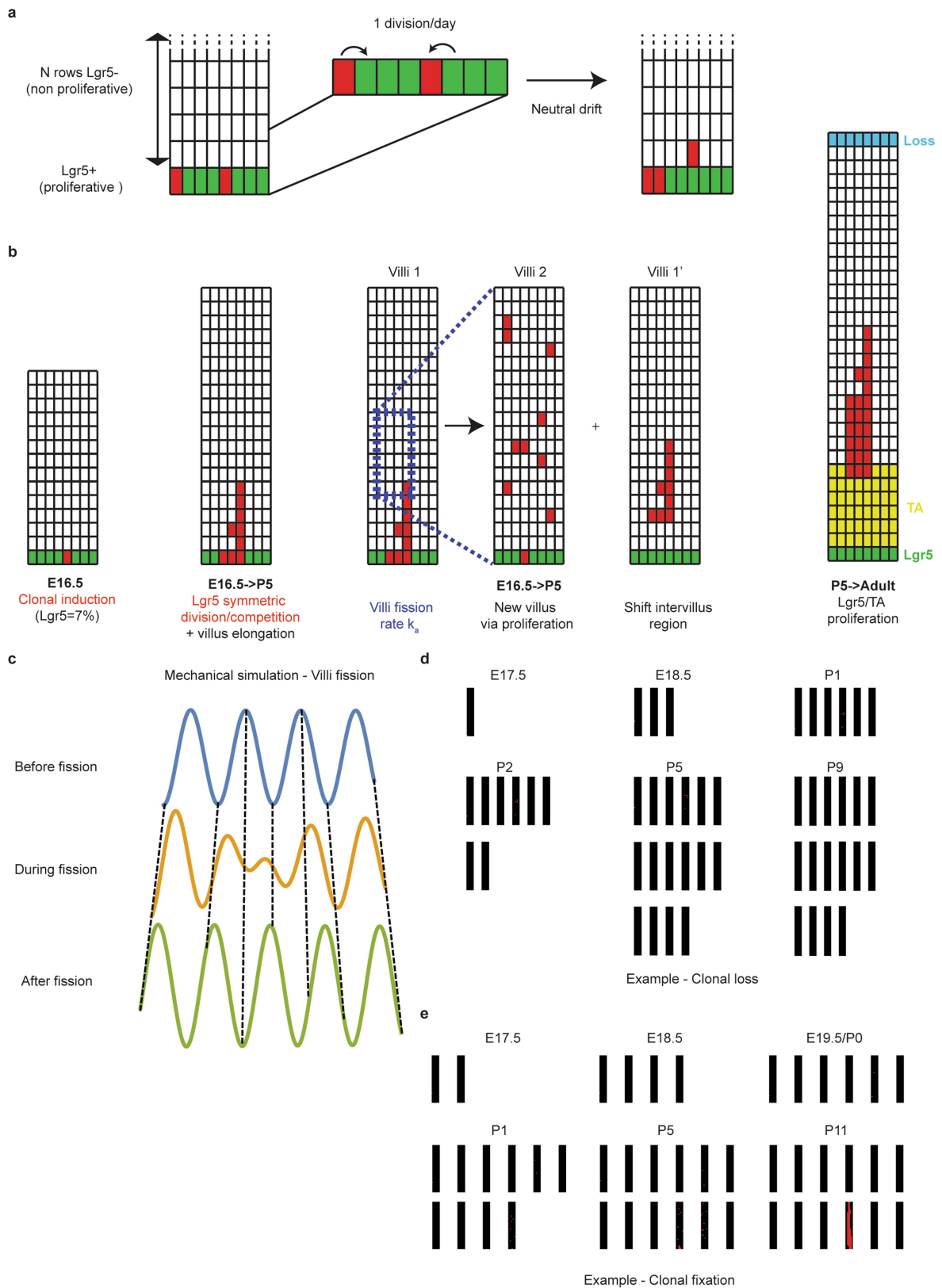
from three mice were analysed and a representative image is shown. **h**, Detection of KRT19 (red) at different time points in tissue from the small intestine. Tissue is counterstained with DAPI (cyan). Scale bars, 50 μ m. Samples from three mice were analysed per time point and representative images are shown. **i**, Relative volume (projected) of KRT19 clones and epithelium based on E-cadherin. E-cadherin is also shown in Fig. 1c and KRT19 clones are also shown in Fig. 2. KRT19 clones, number of biologically independent samples: P0 $n = 1$; P5 $n = 3$, P11 $n = 6$, adult $n = 3$; E-cadherin, number of biologically independent samples: P0 $n = 9$, P5 $n = 9$, P11 $n = 9$, adult $n = 9$. **j**, Quantification of the localization of labelled clones at P0 following administration of 4-hydroxytamoxifen at E16.5 in *Rosa26-lsl-Confetti;Krt19-creER^T* mice. Villi containing clones were divided in three equal regions (T, top; M, middle; B, bottom) based on the z projection in 3D to determine where clones were located at P0 ($n = 27$). **k**, Detection of GFP (green) and RFP (red) in whole mounts from the proximal part of the small intestine isolated from *mT/mG Krt19-creER^T* mice at P0 following induction at E16.5. A representative image of $n = 3$ biologically independent samples is shown. Scale bars, 25 μ m. **l**, Apoptotic cells were detected by cleaved caspase-3. Arrowheads demarcate positive cells in inserts. Samples from three mice were analysed per time point and representative pictures are shown. Scale bars, 250 μ m.



Extended Data Fig. 4 | See next page for caption.

Extended Data Fig. 4 | Villi formation and parameter description of villi fissions. **a**, Total number of villi (projected) in the proximal half of the small intestine based on equal density along the length. Samples from three mice were analysed per time point. Each dot represents a mouse; data are mean \pm s.e.m. **b**, The fold change in villi numbers between the indicated time points based on three samples analysed per time point. Each dot represents an independent sample and lines represent the mean \pm s.e.m. **c**, Villus height at the different time points. The demarcated red lines indicate the interval containing villi with sharing stroma. The length was assessed in 25 villi per mouse and in 3 mice per time point. Dots represent independent measurements and lines represent the mean. **d**, Quantification of the number of villi sharing stroma in three mice per indicated time point (E16.5 $n = 233$, P0 $n = 412$, P5 $n = 406$, P11 $n = 412$, adult $n = 129$ villi were counted). Dots represent the percentage of villi sharing stroma in each independent mouse and the line represents the mean. **e**, Detection of E-cadherin (red) and PDGFRA (yellow) in whole mounts indicating villi with sharing stroma (arrowhead). Samples from three mice were analysed per time point and representative images are shown. Scale bars, 100 μm . **f**, Detection of E-cadherin (magenta) and GFP (*Lgr5-DTR-eGFP*) in E16.5 intestinal whole mount. Boxed area (1) indicates a villus undergoing fission, which is shown at higher magnification (middle). Transverse sections (2 and 3) illustrating villi surrounded by LGR5-expressing cells

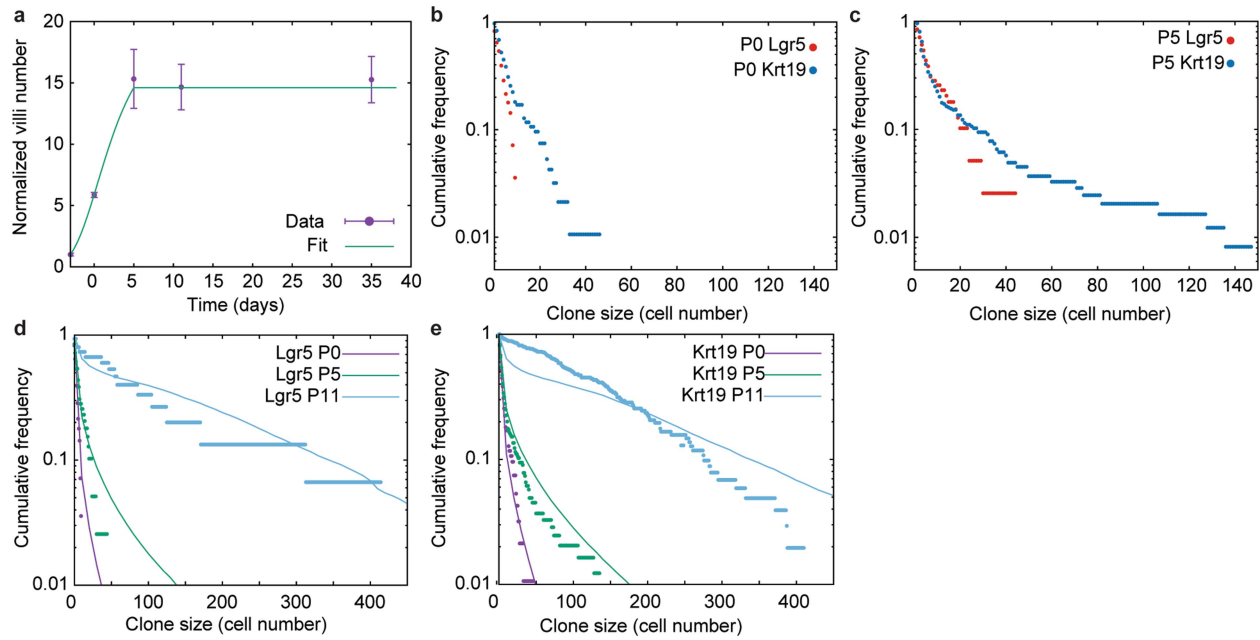
(2) and villus with shared mesenchyme (3). The arrowhead indicates that pockets formed in a fissioning villus are LGR5-negative, the dashed line outlines the epithelium. Samples from three mice were analysed and a representative image is shown. **g**, Detection of EdU incorporation (green) in the epithelium (E-cadherin, red) following a 1-h chase in E16.5 intestinal whole mounts. Arrowheads indicate proliferative cells at the edge of putative villi undergoing fission. These are detected in 11 out of 16 structures. Representative pictures from three mice analysed are shown. Scale bars, 50 μm . **h**, Quantification of EdU intensity in the fissioning areas compared to the surrounding villi at the same height quantified as depicted in the cartoon on the basis of thresholded intensity in the demarcated boxes. $n = 16$ independent villi sharing stroma were quantified. Box plots show the median, box edges represent the first and third quartiles, and the whiskers extend to minimum and maximum values. Dots represent fluorescent ratio of the independent villi sharing stroma. Paired *t*-test. **i**, Height of the proliferative fissioning areas compared to the surrounding intervillus regions were quantified as depicted in the cartoon. $n = 11$ independent villi sharing stroma were quantified. **j**, Images showing the start and end points from live imaging of villi undergoing fission (Supplementary Video 6). Image from *mT/mG; Villin-cre* mice, where the epithelium is shown Green (mG) and remaining cells in red (mT). A representative fission event from five analysed mice is shown. Scale bar, 50 μm .



Extended Data Fig. 5 | See next page for caption.

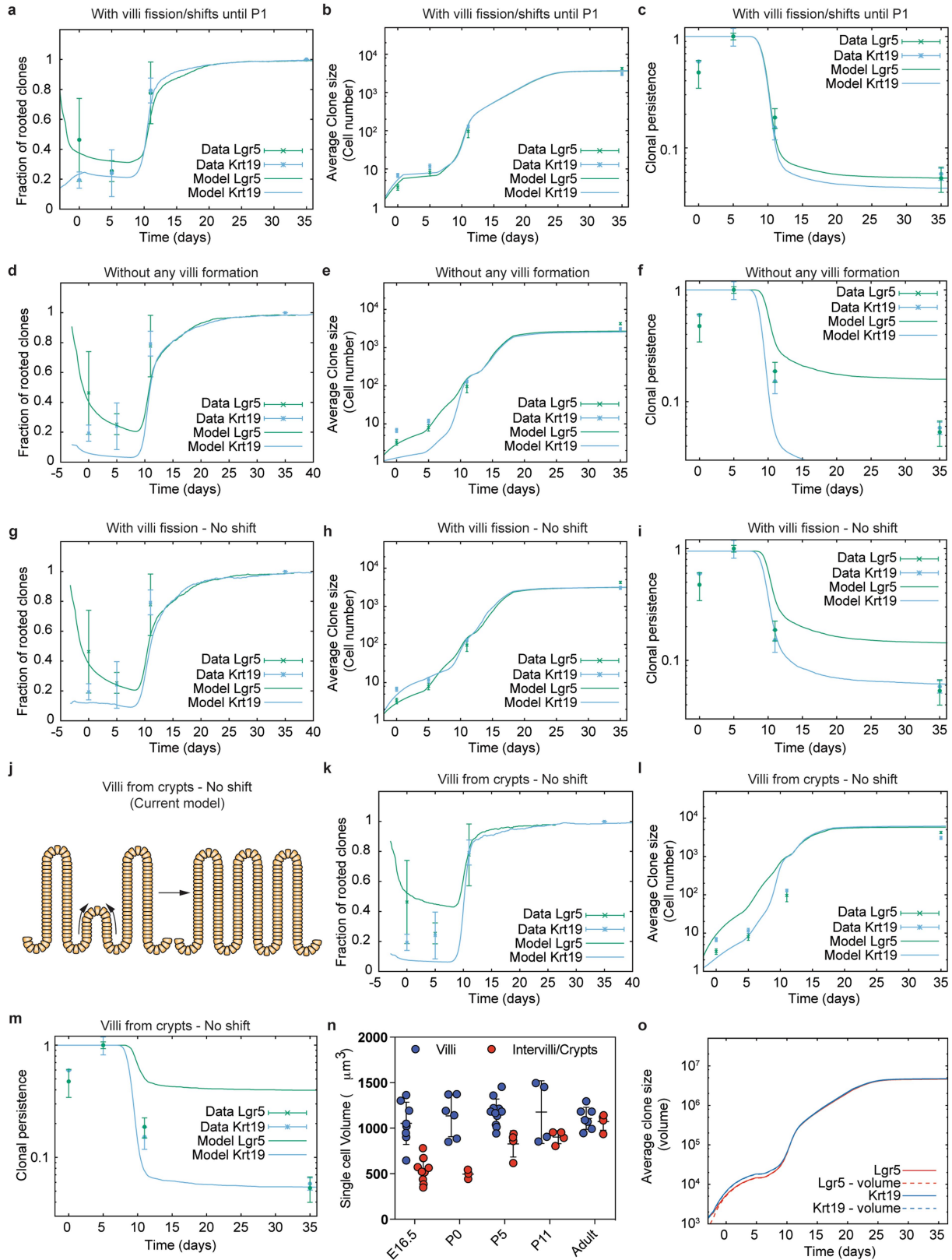
Extended Data Fig. 5 | Outline of the model and typical outputs from simulations. **a**, Schematics of the model for the renewal of intervillus LGR5⁺ cells. On the basis of proliferation data, we assume that the classical model of symmetrically dividing and competing LGR5⁺ cells holds embryonically, with a division rate once a day. The ‘losing’ cell is expelled into the transit-amplifying (TA) compartment, displacing all cells above it by one position. **b**, Schematics of the model for the dynamics of differentiated cells on the villus. The model dynamics are separated into two phases. The first phase occurs from E16.5 to P5: LGR5⁺ cells are the only proliferative cells, and villi fission occurs as a stochastic event, resulting in the duplication of a villus subregion into a whole new intervillus–villus grid, and a resulting shift of cells along the existing villus. A second phase occurs after P5: the dynamics are similar to adulthood, with rapidly dividing transit-amplifying cells (occupying 1/5th of the villus at the bottom) and cell loss at the top. Proliferation of transit-amplifying cells is again exclusively along the top–bottom axis, resulting in unidirectional displacement of all cells above the dividing cell. **c**, Three snapshots from a numerical simulation of the epithelium as a growing

elastic sheet on a growing elastic medium. The growth is assumed to be quasi-static, so that the epithelium maintains a deformation at a given wavelength, minimizing the elastic energy of the sheet and substrate. Where the system grows (top to bottom panels), this results in de novo villi formation from local deformations of the epithelial sheet, resulting in villus and intervillus regions shifting places via tissue bending (the dashed lines serve as a guide to represent how a cell in a given position x can change height z). **d**, **e**, Two sets of snapshots from two numerical simulations of an E16.5 LGR5 tracing, according to the rules outlined in **a**, **b**. Each black box represents an intervillus–villus grid, with the number increasing in time owing to random villi fission. Red squares indicate the labelled cells at E16.5 (initially in the bottom-most layer of LGR5⁺ cells). An example of a clone that becomes lost in time, despite having participated in villi fission between E18.5 and P1 is shown in **d**. An example of a clone that becomes fixed within one of the villi having formed de novo during the simulation (while the labelled cell in the original intervillus–villus region of induction was shifted away from the intervillus by a villi fission event between E16.5 and E17.5) is shown in **e**.



Extended Data Fig. 6 | Clone size distributions based on simulation using the cell-repositioning model. **a**, Total number of intestinal villi over time (purple, same as Extended Data Fig. 4a) normalized against the fitted trend for the villi formation rate (green line), which we use in the numerical simulations. Samples from three mice were analysed per time point. Data are mean \pm s.e.m. **b**, Cumulative distribution of clone sizes (induced at E16.5) at P0 in the LGR5 (red) compared to the KRT19 (blue) tracing (also depicted in Fig. 2d). **c**, Cumulative distribution of clone sizes (induced at E16.5) at P5 in the LGR5 (red) compared to the

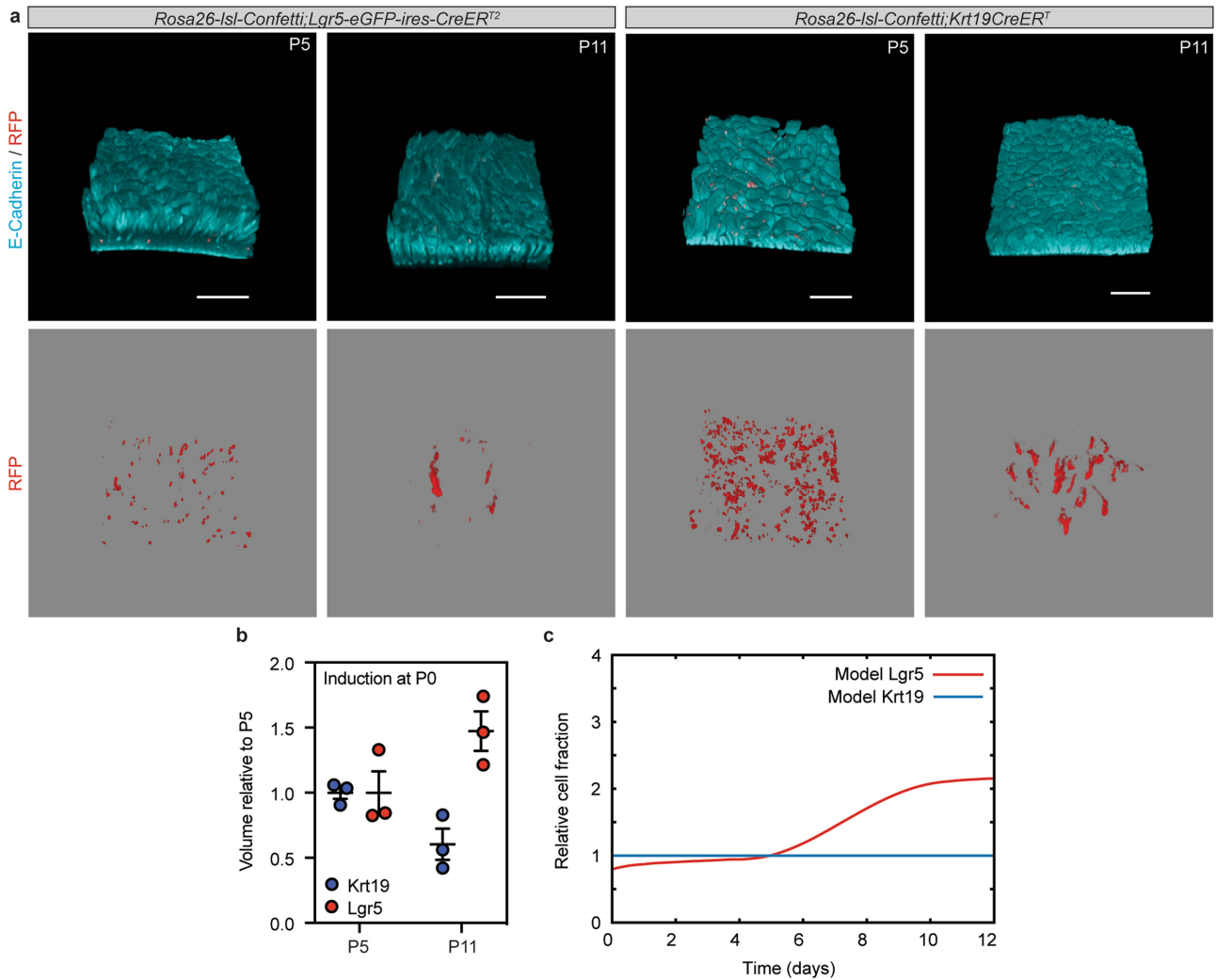
KRT19 (blue) tracing also depicted in Fig. 2d. **d**, Comparison between experimental (dots) and theoretical cumulative distribution of LGR5 clone sizes (induced at E16.5) at P0 (purple), P5 (red) and P11 (cyan). **e**, Comparison between experimental (dots) and theoretical cumulative distribution of KRT19 clone sizes (induced at E16.5) at P0 (purple), P5 (red) and P11 (cyan). For all panels, clone size was inferred from clonal volume (Supplementary Table 2), using average single-cell measurements of volume as a conversion factor.



Extended Data Fig. 7 | See next page for caption.

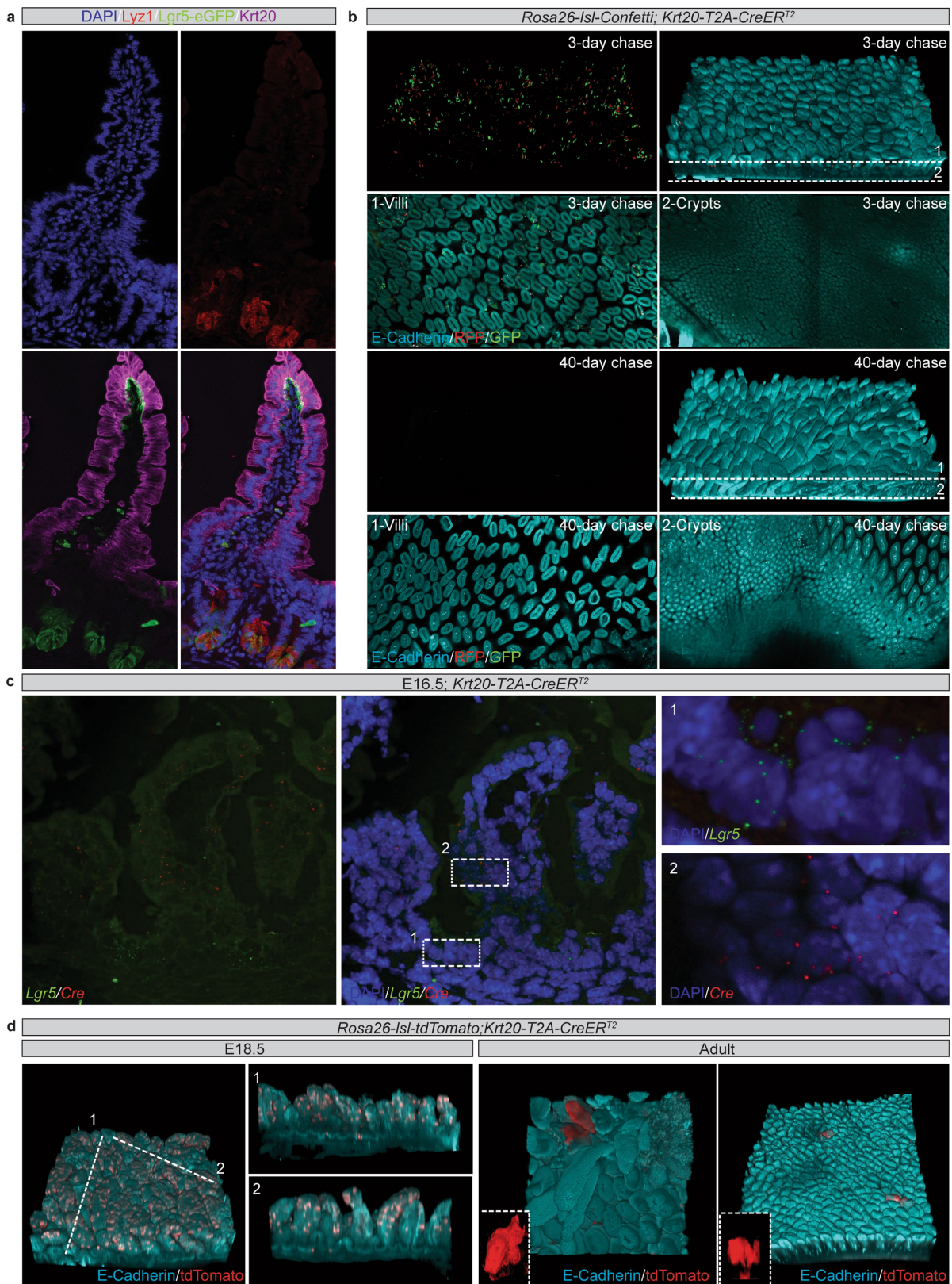
Extended Data Fig. 7 | Theoretical controls and sensitivity analysis. **a–c**, Comparison between experimental data (dots and error bars) and theoretical predictions (thick lines) for the time evolution of the clonal rootedness (**a**), average clone size (**b**) and clonal persistence (**c**), for both KRT19 (cyan) and the LGR5 (green) tracings from E16.5. Here, the theoretical prediction corresponds to the case of villi fission, following exactly the same model in Extended Data Fig. 6, but stopping at P1 instead of at P5. This shows that fetal fission is enough to explain the bulk of the equipotency between LGR5 and KRT19 clones. **d–f**, Comparison between experimental data (dots and error bars) and theoretical predictions (thick lines) for the time evolution of the clonal rootedness (**d**), average clone size (**e**) and clonal persistence (**f**), for both KRT19 (cyan) and LGR5 (green) tracings from E16.5. Here, the theoretical prediction corresponds to the case of no new villi formation occurring, showing a very poor fit for the clonal persistence and size to the data. **g–i**, Comparison between experimental data (dots and error bars) and theoretical predictions (thick lines) for the time evolution of the clonal rootedness (**g**), average clone size (**h**) and clonal persistence (**i**), for both KRT19 (cyan) and LGR5 (green) tracings from E16.5. Here, the theoretical prediction corresponds to the case of villi fission occurring as in the model shown in Fig. 3, but without a shift of cells upon villi fission (see schematics in Extended Data Fig. 5), showing a very poor fit for the clonal persistence to the data. **j**, Cartoon

illustrating that the current villification model suggests that villi emerge from the intervillus region. **k–m**, Comparison between experimental data (dots and error bars) and theoretical predictions (thick lines) for the time evolution of the clonal rootedness (**k**), average clone size (**l**) and clonal persistence (**m**), for both KRT19 (cyan) and LGR5 (green) tracings from E16.5. Here, the theoretical prediction corresponds to the case of villi formation occurring only from existing crypts, showing a very poor fit for the clonal persistence to the data. **n**, Volume of single villus cells and intervillus–crypts cells. Total E-cadherin volume of villi and intervillus–crypts, subsequently divided by the number of DAPI⁺ nuclei to estimate single-cell volume. E16.5 villi $n = 8$, E16.5 intervilli $n = 10$, P0 villi $n = 6$, P0 intervilli $n = 3$, P5 villi $n = 11$, P5 intervilli $n = 4$, P11 villi $n = 4$, P11 intervilli $n = 4$, adult villi $n = 7$, adult intervilli $n = 4$ independent images were analysed. **o**, Sensitivity analysis on the influence of differential LGR5⁻ and LGR5⁺ cellular volume on the model prediction—considering either that all cells have the same volume (continuous lines and **a–n**) or the differential volume measured at E16.5 (see Supplementary Theory Note, dashed lines). For **a–i**, **k–m**: P0 $n = 3$, P5 $n = 3$, P11 $n = 3$, adult $n = 6$ independent samples analysed for LGR5; P0 $n = 1$, P5 $n = 3$, P11 $n = 6$, adult $n = 3$ independent samples analysed for KRT19. Data are mean \pm s.e.m.



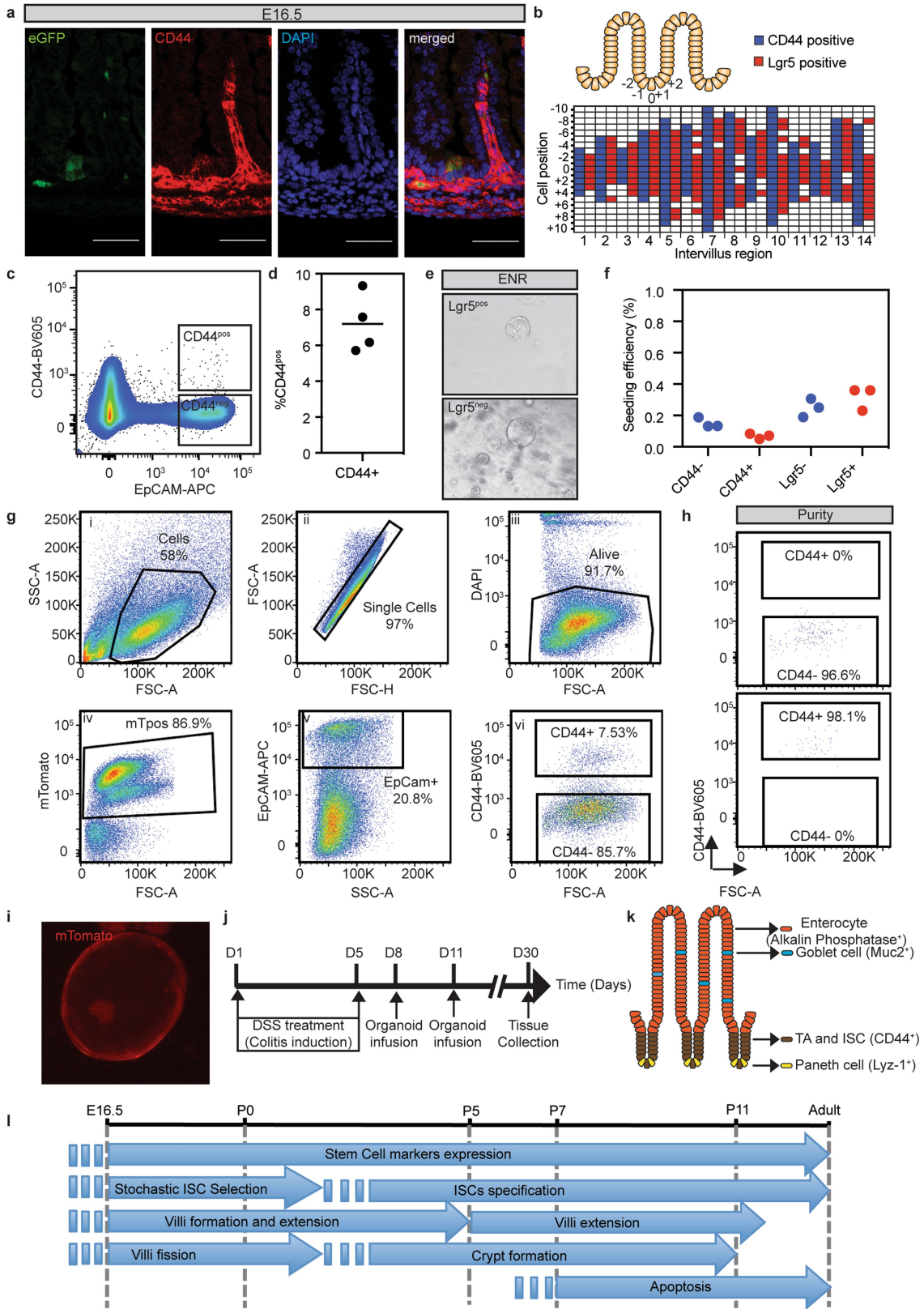
Extended Data Fig. 8 | Postnatal lineage tracing. **a**, Detection of E-cadherin (cyan) and clones (red) induced at P0 either randomly (*Krt19-creER^T*) or in the intervillus region (*Lgr5-eGFP-ires-creER^{T2}*). Samples from three mice were analysed per time point and representative images are shown. **b**, Relative volume of clones (projected) induced either randomly (*Krt19-creER^T*) or in the intervillus region (*Lgr5-eGFP-ires-creER^{T2}*) as assessed by quantitative clonal analysis following induction at P0. Samples from three mice were analysed per time point and dots

represent individual samples and lines indicate the mean \pm s.e.m. **c**, Theoretical labelled-cell fraction of the LGR5 clones induced at P0, using the same model dynamics as the E16.5 induction. Expansion of the LGR5 clones is represented by the thick red line, normalized to the Krt19 tracing (blue, indicative of global tissue growth) and to its P5 value. This displays a net twofold increase between P5 and P11, consistent with the results of the experimental P0 tracing.



Extended Data Fig. 9 | The contribution of KRT20-expressing cells during development and homeostasis. **a**, Detection of keratin 20 (KRT20, magenta), lysozyme1 (LYZ1, red) and GFP (*Lgr5-DTR-eGFP*) in adult mouse intestine. Tissue is counterstained with DAPI (cyan). Representative image of $n = 3$ biologically independent samples is shown. **b**, Detection of E-cadherin (cyan), GFP (green) and RFP (red) in tissue whole mounts from the proximal part of the small intestine isolated from *Rosa26-IsI-Confetti;Krt20-T2A-creER^{T2}* mice at 3 and 40 days after label induction with 4-hydroxytamoxifen. Samples from three

mice were analysed per time point and representative images are shown. **c**, In situ hybridization of *Lgr5* (green) and *cre* (red) in proximal E16.5 small intestine. Tissue is counterstained with DAPI (cyan). Samples from three mice were analysed per time point and representative images are shown. **d**, Detection of E-cadherin (cyan) and tdTomato (red) in tissue whole mounts from the proximal small intestine isolated from *Rosa26-IsI-tdTomato;Krt20-T2A-creER^{T2}* mice at E18.5 and adulthood following administration of 4-hydroxytamoxifen at E16.5. Representative images of $n = 2$ samples are shown.



Extended Data Fig. 10 | See next page for caption.

Extended Data Fig. 10 | Testing intestinal epithelial cells for

equipotency. a, Detection of LGR5-eGFP (green) and CD44 (red) in the E16.5 small intestine isolated from *Lgr5-eGFP-ires-creER^{T2}* E16.5 mice.

Tissue was counterstained with DAPI (blue). Samples from three mice were analysed and a representative image is shown. Scale bars, 50 μm .

b, Cartoon showing the positions used to quantify the pattern of CD44 and LGR5 expression. Quantification of the localization of CD44 and LGR5 positive cells. A total of 14 intervillus regions (x axis) were quantified up to position ± 10 (y axis).

c, d, Representative FACS dot plot illustrating the gating strategy used to quantify CD44. Dots represent the quantification in individual mice ($n = 4$). **e,** Spheroids forming from cells isolated based on DAPI⁻EpCAM⁺LGR5-eGFP⁻ and DAPI⁻EpCAM⁺LGR5-eGFP⁻ from the proximal half of the small intestine from mice at E16.5. Representative

images of $n = 3$ biologically independent samples. **f,** Quantification of spheroid seeding efficiency following isolation based on either CD44 or LGR5 ($n = 3$ mice per condition). **g-i,** Gating strategy for purification of villus and intervillus cells for transplantation. The gating hierarchy of the panels is numbered i-vi (**g**), an example of purity is indicated (**h**) and an mT/mG-derived organoid is shown (**i**). Spheroids were generated from a pool of $n = 6$ biologically independent samples. **j, k,** Outline for transplantation experiment. In brief, experimental colitis was induced in *RAG2^{-/-}* mice by administration of DSS in the drinking water. Organoids from the different cultures were subsequently infused into lumen of the mice (**j**) and engrafted regions were immunostained for lineage and stem-cell markers (**k**). **l,** Scheme summarizing the main findings of this work.

Reporting Summary

Nature Research wishes to improve the reproducibility of the work that we publish. This form provides structure for consistency and transparency in reporting. For further information on Nature Research policies, see [Authors & Referees](#) and the [Editorial Policy Checklist](#).

Statistics

For all statistical analyses, confirm that the following items are present in the figure legend, table legend, main text, or Methods section.

n/a Confirmed

- The exact sample size (n) for each experimental group/condition, given as a discrete number and unit of measurement
- A statement on whether measurements were taken from distinct samples or whether the same sample was measured repeatedly
- The statistical test(s) used AND whether they are one- or two-sided
Only common tests should be described solely by name; describe more complex techniques in the Methods section.
- A description of all covariates tested
- A description of any assumptions or corrections, such as tests of normality and adjustment for multiple comparisons
- A full description of the statistical parameters including central tendency (e.g. means) or other basic estimates (e.g. regression coefficient) AND variation (e.g. standard deviation) or associated estimates of uncertainty (e.g. confidence intervals)
- For null hypothesis testing, the test statistic (e.g. F , t , r) with confidence intervals, effect sizes, degrees of freedom and P value noted
Give P values as exact values whenever suitable.
- For Bayesian analysis, information on the choice of priors and Markov chain Monte Carlo settings
- For hierarchical and complex designs, identification of the appropriate level for tests and full reporting of outcomes
- Estimates of effect sizes (e.g. Cohen's d , Pearson's r), indicating how they were calculated

Our web collection on [statistics for biologists](#) contains articles on many of the points above.

Software and code

Policy information about [availability of computer code](#)

Data collection

Image acquiring
-NDP Zoomer Digital Pathology (Hamamatsu).scan
-LAS X
-LAS EZ
-LAS v3.8
-Zeiss ZEN 2.3
-SoftWorx 6.5.2

Flow cytometry
-BD FACS DIVA

Data analysis

The numerical simulations used for the theoretical modelling were performed using a custom code in C++, provided with this submission.

Image processing:
-Fiji (version 2.0.0-rc-39/1.50b)
-Adobe Photoshop CS6 (13.0.6x64)
-NDP view2

Clones quantification:
-Volocity 6.3.0 (Perkin Elmer)

Flow cytometry:
-FlowJo 10.1r5

scRNAseq:
 -10x Genomics Cellranger 2.1.0
 - Pagoda 2
 - Seurat 2.3

Graph Generation and data analysis:
 -GraphPad Prism 7
 -Excel 2011

For manuscripts utilizing custom algorithms or software that are central to the research but not yet described in published literature, software must be made available to editors/reviewers. We strongly encourage code deposition in a community repository (e.g. GitHub). See the Nature Research [guidelines for submitting code & software](#) for further information.

Data

Policy information about [availability of data](#)

All manuscripts must include a [data availability statement](#). This statement should provide the following information, where applicable:

- Accession codes, unique identifiers, or web links for publicly available datasets
- A list of figures that have associated raw data
- A description of any restrictions on data availability

RNA sequencing data that support the findings of this study have been deposited in the ArrayExpress database at EMBL-EBI (www.ebi.ac.uk/arrayexpress) under accession number EMTAB-7660. All other data supporting the findings of this study are available from the corresponding author on reasonable request.

Field-specific reporting

Please select the one below that is the best fit for your research. If you are not sure, read the appropriate sections before making your selection.

Life sciences Behavioural & social sciences Ecological, evolutionary & environmental sciences

For a reference copy of the document with all sections, see nature.com/documents/nr-reporting-summary-flat.pdf

Life sciences study design

All studies must disclose on these points even when the disclosure is negative.

Sample size	Sample size was determined based on our experience and previous experiments.
Data exclusions	No data were excluded from the analysis
Replication	Experimental data was replicated using at least 3 independent biological samples (Precisely stated in the figure legends), except for Human fetal intestine that was only performed twice with reliable results. There were no attempts at replication that failed.
Randomization	Randomized cohorts including both male and female animals were distributed in an unblinded manner into the experimental time points for analysis
Blinding	No blinding was used because embryos had to be genotyped by PCR and/or under the fluorescent stereoscope before whole mount immunostainings.

Reporting for specific materials, systems and methods

We require information from authors about some types of materials, experimental systems and methods used in many studies. Here, indicate whether each material, system or method listed is relevant to your study. If you are not sure if a list item applies to your research, read the appropriate section before selecting a response.

Materials & experimental systems

n/a	Involved in the study
<input type="checkbox"/>	<input checked="" type="checkbox"/> Antibodies
<input checked="" type="checkbox"/>	<input type="checkbox"/> Eukaryotic cell lines
<input checked="" type="checkbox"/>	<input type="checkbox"/> Palaeontology
<input type="checkbox"/>	<input checked="" type="checkbox"/> Animals and other organisms
<input type="checkbox"/>	<input checked="" type="checkbox"/> Human research participants
<input checked="" type="checkbox"/>	<input type="checkbox"/> Clinical data

Methods

n/a	Involved in the study
<input checked="" type="checkbox"/>	<input type="checkbox"/> ChIP-seq
<input type="checkbox"/>	<input checked="" type="checkbox"/> Flow cytometry
<input checked="" type="checkbox"/>	<input type="checkbox"/> MRI-based neuroimaging

Antibodies

Antibodies used

-Impress HRP Anti-Rabbit IgG, Ready to use, Vector (MP-7401)
 -Anti-ChromograninA, Rabbit Polyclonal, 1/300, Abcam (ab15160)
 -Anti-GFP antibody, Chicken polyclonal, 1/300 Abcam (ab13970)
 -anti-RFP, Rabbit, 1/300, Rockland (600401379)
 -Purified Mouse Anti-E-Cadherin Clone 36, 1/300, BD bioscience (610181)
 -Cleaved caspase-3 (D175), rabbit, 1/300, Cell Signalling (#9661)
 -Lysozyme 1(EC.3.2.1.17), 1/500, Dako (A0099)
 -Muc2 (H-300), 1/300, Santa Cruz (sc-15334)
 -CD44 (clone IM7) 1/50 Pharmingen (563058)
 -CD44v6 (9A4) 1/100 Serotec (MCA1967)
 -CD140a, PDGF Receptor a (Clone APA5) 1/50 (FACS); 1/300 (Immunofluorescence) eBioscience (25-1401-80)
 -EpCAM (clone G8.8) 1/50 eBioscience (17-5791-80)
 -CD45 (clone 30F-11) 1/50 BD Pharmingen (552848)
 -CD31 (clone 390) 1/50 eBioscience (561410)
 -Cytokeratin19 rabbit 1/300 abcam (ab15463)
 -Cytokeratin 19 (A-3): sc-376126 1/300 Santa Cruz
 -anti-Keratin K20 1/500 Progen (GP-K20)
 -Alexa Fluor 488 Goat anti-Chicken IgY (H+L) 1/500 Thermo Fisher (A-11039)
 -Alexa Fluor 555 Donkey anti Rabbit IgG (H+L) 1/500 Thermo Fisher (A-31572)
 -Alexa Fluor 488 Donkey anti Rat IgG (H+L) 1/500 Thermo Fisher (A-21208)
 -Alexa Fluor 647 Goat anti mouse IgG2a 1/500 Thermo Fisher (A-21241)
 -Alexa Fluor 555 Goat anti-Guinea Pig IgG (H+L) 1/500 Thermo Fisher (A18769)

All materials are available except Muc2 antibody that has been discontinued.

Validation

The antibodies used were validated by independent publications and/or by the supplier (see information below). Negative control stainings (only secondary antibody) were done as a control.

The antibodies used are also specified in Supplementary Table1.

-Anti-ChromograninA, Abcam (ab15160): <https://www.abcam.com/chromogranin-a-antibody-ab15160-references.html#active-tab>

-Anti-GFP antibody, Abcam (ab13970): <https://www.abcam.com/gfp-antibody-ab13970-references.html#top-356>

-anti-RFP, Rockland (600401379): <https://rockland-inc.com/Product.aspx?id=40760>

-Purified Mouse Anti-E-Cadherin Clone 36BD bioscience (610181): <http://www.bdbiosciences.com/eu/applications/research/stem-cell-research/cancer-research/human/purified-mouse-anti-e-cadherin-36e-cadherin/p/610181>

-Cleaved caspase-3 (D175), rabbit, Cell Signalling (#9661): <https://www.cellsignal.com/products/primary-antibodies/cleaved-caspase-3-asp175-antibody/9661>

-Lysozyme 1(EC.3.2.1.17), Dako (A0099): [https://www.agilent.com/en/product/immunohistochemistry/antibodies-controls/primary-antibodies/lysozyme-ec-3-2-1-17-\(concentrate\)-76124#specifications](https://www.agilent.com/en/product/immunohistochemistry/antibodies-controls/primary-antibodies/lysozyme-ec-3-2-1-17-(concentrate)-76124#specifications)

-Muc2 (H-300), 1/300, Santa Cruz (sc-15334): <https://www.scbt.com/scbt/product/mucin-2-antibody-h-300>

-CD44 (clone IM7), Pharmingen (563058): <http://www.bdbiosciences.com/cn/applications/research/stem-cell-research/cancer-research/mouse/bv605-rat-anti-mouse-cd44-im7/p/563058>

-CD44v6 (9A4), Serotec (MCA1967): <https://www.bio-rad-antibodies.com/monoclonal/mouse-cd44v6-antibody-9a4-mca1967.html?f=purified>

-CD140a, PDGF Receptor a (Clone APA5), eBioscience (25-1401-80): <https://www.thermofisher.com/antibody/product/CD140a-PDGFRA-Antibody-clone-APA5-Monoclonal/25-1401-82>

-EpCAM (clone G8.8), eBioscience (17-5791-80): <https://www.thermofisher.com/antibody/product/CD326-EpCAM-Antibody-clone-G8-8-Monoclonal/17-5791-82>

-CD45 (clone 30F-11), BD Pharmingen (552848): <http://www.bdbiosciences.com/eu/applications/research/stem-cell-research/cancer-research/mouse/pe-cy7-rat-anti-mouse-cd45-30-f11/p/552848>

-CD31 (clone 390), eBioscience (561410): <http://www.bdbiosciences.com/eu/applications/research/stem-cell-research/cancer-research/mouse/pe-cy7-rat-anti-mouse-cd31-390/p/561410>

-Cytokeratin19 rabbit abcam (ab15463); <https://www.abcam.com/cytokeratin-19-antibody-ab15463.html>

-Cytokeratin 19 (A-3), sc-376126 Santa Cruz: <https://www.scbt.com/scbt/product/cytokeratin-19-antibody-a-3>

-anti-Keratin K20 1/500 Progen (GP-K20): <https://www.progen.com/anti-keratin-k20-guinea-pig-polyclonal-serum.html>

Animals and other organisms

Policy information about [studies involving animals](#); [ARRIVE guidelines](#) recommended for reporting animal research

Laboratory animals	<p>Mus musculus was used as an animal model.</p> <p>The strains indicated below were used:</p> <ul style="list-style-type: none"> -C57BL/6J mice purchased from Taconic -Gt(ROSA)26Sortm4(ACTB-tdTomato,-EGFP)Luo/J (mT/mG) -Lgr5-eGFP-ires-CreERT2 -Krt19CreRT -RAG2-/- (Purchased from Taconic) -CD1 (Purchased from Janvier) -Rosa26-IsI-tdTomato -Lgr5-DTR-eGFP -Krt20-T2A-CreERT2 -Villin-Cre <p>Males and females were used for the study. Animals were analyzed at: E14.5, E16.5, P0, P5, P11 and Adult stages.</p> <p>All animals were housed in SPF (specific pathogen free) animal facilities, in either open or individually ventilated cages always with companion mice, and cages were placed under a 12hr light-dark cycle. Food and water were provided ad libitum.</p>
Wild animals	No wild animals were used
Field-collected samples	The study did not involved samples collected from the field
Ethics oversight	The National animal ethics committee in Denmark reviewed and approved all animal procedures (Permit numbers 2013-15-2934-00756 and 2013-15-2934-00927).

Note that full information on the approval of the study protocol must also be provided in the manuscript.

Human research participants

Policy information about [studies involving human research participants](#)

Population characteristics	Smoker and non-smoker pregnant women.
Recruitment	Human fetal intestinal samples were used in this study. Women gave their informed written and oral consent. None of the terminations were for reasons of fetal abnormality and the fetal tissue was available following elective termination of pregnancy during first trimester. Potential selection biases were not detected/observed.
Ethics oversight	Human fetal tissue collection was approved by the regional ethics committee (permit number H-1-2012-007 and 258206).

Note that full information on the approval of the study protocol must also be provided in the manuscript.

Flow Cytometry

Plots

Confirm that:

- The axis labels state the marker and fluorochrome used (e.g. CD4-FITC).
- The axis scales are clearly visible. Include numbers along axes only for bottom left plot of group (a 'group' is an analysis of identical markers).
- All plots are contour plots with outliers or pseudocolor plots.
- A numerical value for number of cells or percentage (with statistics) is provided.

Methodology

Sample preparation	<p>In all experiments where Flow cytometry was used (Either from mouse or human origin), samples were prepared as indicated below:</p> <ul style="list-style-type: none"> -Fetal small intestine from mouse or human fetuses was dissected and incubated with collagenase solution (125µg/mL in PBS) for 45 min at 37°C, and subjected to vigorously pipetting every 15 min using a P1000 pipette. Released cells were pelleted and resuspended in PBS supplemented with 1% BSA and incubated with fluorescent conjugated primary antibodies (indicated in Supplementary Table 1) for 30 min on ice. After washing, 4,6-Diamidino-2-phenylindole dihydrochloride (DAPI; Sigma; 1µM) was added to the cell suspension to facilitate exclusion of dead cells by flow cytometry.
Instrument	FACSAria I or III (BD Bioscience) were used indistinctly. LSRII and FACSCanto were use to acquire.
Software	BD FACSDIVA was used to collect the data and FlowJo to analyze it

Cell population abundance

The purity of the samples was assessed in the sorting experiments, the results are indicated below:

- In Organoid efficiency experiments (Figure 4a,b) the purity was >91% (CD44positive cells and CD44negative cells) and >96% (Lgr5positive cells and Lgr5negative cells).
- In human fetal intestinal experiments (Figure 4c) the purity was >97% (CD44positive cells and CD44negative cells)
- In transplantation experiments (Figure 4d) the purity was >98% (CD44positive cells and CD44negative cells). The purity of this experiment is shown in Extended Data Figure 10h)

Gating strategy

We used the the gating strategy indicated below:

- GFP quantification (Extended data figure 2g-h): GFP vs EpCAM from from DAPIneg-CD45neg-CD31neg gate.
- CD44 quantification (Extended data Figure 10c): the plot illustrates CD44 vs EpCam from DAPIneg-CD45neg-CD31neg-PDGFRAneg gate.
- Organoid Plating efficiency and maturation (Figure 4a,b): DAPIneg-EpCAMpos-CD44pos and DAPIneg-EpCAMpos-CD44neg
- Human organoids(Figure 4c): DAPInegCD44pos and DAPInegCD44neg
- Organoids used for intestinal transplantation (Figure 4d): DAPIneg-mTpos-EpCAMposCD44pos and DAPInegEpCAMposCD44neg (This gating strategy is shown in Extended Data Figure 10g

Doublets were excluded using a FSS-H/FSC-A gating strategy.

Unstained samples and single staining controls were always used to define the gate boundaries. When optimizing the techniques used, all minus one controls were used

Tick this box to confirm that a figure exemplifying the gating strategy is provided in the Supplementary Information.